https://doi.org/10.5194/egusphere-2025-5624
Preprint. Discussion started: 26 January 2026

MErSiM v1.0: Resolving Biases in Global Silicate Weathering Model with A Data-Driven Surface Erosion Module

Jiaxi Zhao[1], Yonggang Liu[1,2,3] and Yongyun Hu[1,3]

[1]Laboratory for Climate and Ocean-Atmosphere Studies, Department of Atmospheric and Oceanic Sciences, School of Physics, Peking University, Beijing 100871, China;
[2]Institute of Carbon Neutrality, Peking University, Beijing, China;
[3]Institute of Ocean Research, Peking University, Beijing, China;

Correspondence to: Yonggang Liu (ygliu@pku.edu.cn)

Abstract. The silicate weathering feedback is a key planetary thermostat regulating Earth's long-term climate, yet process-based models of this mechanism suffer from biases. The widely-used weathering model, when driven by stream power erosion laws, systematically overestimates weathering fluxes in the tropics and predicts a global total flux nearly double the observation-based estimates. This study demonstrates that this discrepancy partially originates from a poorly constrained erosion submodule. To resolve this, we developed a new global erosion model using a Random Forest algorithm trained on ~4,000 ^{10}Be-derived, basin-averaged erosion rates. Our data-driven model explains 90% of the variance in the observational erosion data, far exceeding the performance of the traditional Stream Power Incision Model (SPIM) and other existing approaches. By integrating this newly developed erosion module into a commonly used framework, we created a revised silicate weathering model, named MErSiM v1.0 (Machine-learning derived Erosion and Silicate-weathering Model). This new model successfully eliminates the systematic tropical overestimation, and its predicted global total flux (~3.1×10^{12} mol C yr^{-1}) is now in better agreement with observations. More fundamentally, MErSiM resolves a critical trade-off in the original framework, now able to simultaneously match both the global total flux and the watershed-scale spatial pattern of weathering. Sensitivity experiments reveal that while MErSiM's response to glacial-interglacial climate change is comparable to previous work, its feedback to intense warming ($4\times CO_2$) is profoundly attenuated (a 42% increase vs. 149% in the original model). This dampened sensitivity stems from a structural shift to a more supply-limited weathering regime, a finding supported by a newly calibrated set of "sluggish" chemical kinetic parameters. This work delivers a comprehensively evaluated and observationally constrained model, which suggests that the silicate weathering feedback may be a weaker climate stabilizer under extreme greenhouse conditions than previously thought.

https://doi.org/10.5194/egusphere-2025-5624
Preprint. Discussion started: 26 January 2026

1 Introduction

The chemical weathering of silicate minerals on the Earth's continents one of the primary sinks for atmospheric carbon dioxide (CO_2) on geological timescales (Berner et al., 1983; Walker et al., 1981). This process acts as a planetary thermostat, modulating global climate by providing a negative feedback loop: warmer, wetter conditions tend to accelerate weathering rates, leading to increased CO_2 consumption and subsequent cooling (Brantley et al., 2023; Raymo and Ruddiman, 1993). Understanding the controls on silicate weathering is therefore fundamental to resolving the causes of past climate evolution, such as the long-term cooling trend throughout the Cenozoic, and to assessing the stability of the Earth system in the face of perturbations (Kump et al., 2000; Maher and Chamberlain, 2014).

Numerical modeling provides an indispensable tool for quantifying weathering fluxes, especially for deep-time scenarios where direct measurements are challenging. Early models, from zero-dimensional frameworks like GEOCARB (Berner, 1991), to subsequent two-dimensional models such as the Gibbs and Kump Weathering Model (GKWM) (Bluth and Kump, 1994), the Global Erosion Model for CO2 fluxes (GEM-CO2) (Amiotte Suchet et al., 2003) and a model by Hartmann (Hartmann et al., 2009; Hartmann and Moosdorf, 2012) identified lithology and runoff as dominant controls on weathering. However, compilations of modern river basin data revealed that the spatial variability of weathering required a combined explanation of runoff, temperature, and crucially, physical erosion rates (Gaillardet et al., 1999).

A major conceptual breakthrough came from West et al. (2005), who formalized the dual-control framework of weathering regimes. In transport- or supply-limited settings, typically flat, low-relief terrains, the rate of chemical transformation is constrained by the slow physical supply of fresh minerals to the weathering front, a process governed by the erosion rate (Fig. 1a). Conversely, in kinetic-limited settings, such as steep, rapidly eroding mountains, fresh material is abundant, and the weathering rate is instead limited by the intrinsic speed of chemical reactions, which are sensitive to factors like temperature and water availability (West et al., 2005) (Fig. 1b). This led to the development of the one-dimensional dynamic weathering model by Gabet and Mudd (2009) (hereafter GM09), a process-based model for global silicate weathering. The model's core strength lies in its conceptual framework that the weathering rate (W) is co-limited by two distinct regimes (Fig. 1c). The GM09 model has thus become a popular tool, notably being integrated into larger Earth System Models like GEOCLIM to explore long-term climate-tectonic interactions (Godderis et al., 2017; Park et al., 2020).

https://doi.org/10.5194/egusphere-2025-5624
Preprint. Discussion started: 26 January 2026

Despite its conceptual strengths, evaluations of the GM09 model against modern observational data have revealed some weakness. The calibrated model presented by Park et al. (2020) (hereafter Park20) yields a present-day global silicate weathering flux of ~4.5×10^{12} mol C yr^{-1}. This value nearly doubles the modern flux of ~2.5×10^{12} mol C yr^{-1} estimated from river chemistry compilations (Gaillardet et al., 1999) and also exceeds revised estimates of the modern global volcanic CO_2 outgassing rate (~2–3.3×10^{12} mol C yr^{-1}) (Müller et al., 2022). Such an imbalance is large enough to plunge the planet into an extreme icehouse state within a few million years (Berner and Caldeira, 1997).

Critically, this discrepancy is not randomly distributed over watersheds. It stems from a systematic overestimation of weathering fluxes specifically in tropical regions, a bias also supported by osmium isotope data (Rugenstein et al., 2021). It has been previously shown that this issue of systematic overestimation can be largely mitigated by recalibrating model parameters using alternative goodness-of-fit metrics (e.g., a combination of R^2 and R^2_{log}) (Zuo et al., 2024) but the model's performance at the watershed scale, measured by the correlation between simulated and observed fluxes, remains low. Zuo et al. (2024) further hypothesized that the regional discrepancy originated not from the chemical kinetics component of the model, but from the calculation of surface erosion (E). The predominant importance of erosion on the silicate weathering has also been supported by geochemical evidence (Hilton and West, 2020; Wan et al., 2012). The original GM09 model, and many of its applications, utilize a simplified Stream Power Incision Model (SPIM) to estimate erosion, which may not adequately capture the complex reality of Earth's surface processes. Zuo et al. (2024) noticed that the overestimation in the tropics coincided with the widespread distribution of highly-weathered, erosion-resistant leached soil. By implementing an "patch"—reducing erosion rates by an order of magnitude in areas with high Leaf Area Index (LAI), an approximate proxy for leached soil distribution—they successfully ameliorated both the systematic overestimation and the watershed-scale biases. However, the way in which erosion rate is reduced in the "patching" method is subjective and non-mechanistic, lacking a direct constraint from erosion observations and not generalizable. A more universally applicable and observationally-constrained erosion model is required.

Modeling erosion at the global scale is challenging because it is a complex process governed by a non-linear interplay of multiple factors, including topography, climate, vegetation, and lithology. Previous models, like SPIM or simple slope-based functions, often capture only one aspect of this complexity and exhibit limited explanatory power. To overcome these

https://doi.org/10.5194/egusphere-2025-5624
Preprint. Discussion started: 26 January 2026

limitations, Zhao et al. (2026) turned to a data-driven approach using machine learning. Machine learning algorithms, particularly Random Forest, are exceptionally skilled at learning complex, high-dimensional, and non-linear relationships from data without pre-supposing a fixed functional form. The model of Zhao et al. (2026) performed well on the modern Earth when trained with high-spatial-resolution (~1 km) data, superior to other traditional models (see their Fig. 5), and the resulting nonlinear relationships between erosion and various factors from the model were physically reasonable.

The primary goal of this paper is to develop, describe, and evaluate an improved global silicate weathering model. To achieve this, we pursue the following specific objectives: (1) To develop a new global erosion model using machine learning, with the primary difference from that in Zhao et al. (2026) being much lower spatial resolution is adopted here so that the model will be applicable to studying the deep-time Earth (for example the uplift-weathering hypothesis of late Cenozoic cooling). (2) To integrate this new data-driven erosion module into the GM09 weathering model framework, replacing the original, physically-simplified submodule. (3) To rigorously evaluate the performance of the integrated model against modern observation-based weathering fluxes at both global and watershed scales, demonstrating its ability to resolve the long-standing issue of tropical overestimation.

This paper is structured as follows: Section 2 details the GM09 model, the datasets, and the methodology used to develop and couple the new erosion model. Section 3 presents the results, focusing first on the performance of the new erosion model itself and then on the improved performance of the coupled weathering model. Section 3 also discusses the physical interpretations of our findings and their broader implications for understanding the global carbon cycle and paleoclimate. Finally, Section 4 summarizes our main conclusions.

2 Model and Data

2.1 The Reference Silicate Weathering Model (GM09-SPIM)

Our work improves upon the global silicate weathering model as implemented by Park et al. (2020). This implementation is a transient, time-varying version of the regolith model framework established by GM09. It simulates a chemically weathered profile, or regolith, that forms on top of unweathered bedrock (see Fig. 1). The model tracks the evolution of the regolith through a set of three coupled differential equations.

https://doi.org/10.5194/egusphere-2025-5624
Preprint. Discussion started: 26 January 2026

2.1.1 The Transient Model Formulation

The core of the GM09 model describes the change in regolith thickness (h, in meters) as a balance between the regolith production rate from bedrock (P_r, in m/yr) and the physical erosion rate at the surface (E, in m/yr):

$$\frac{dh}{dt} = P_r - E \quad (1)$$

Simultaneously, the model tracks the evolution of the fractional abundance of weatherable primary minerals (x, unitless) within the regolith. This concentration changes as a function of time (t, yr) and depth (z, m) due to both upward advection with the regolith column and chemical dissolution:

$$\frac{\partial x}{\partial t} = -P_r \left(\frac{\partial x}{\partial z}\right) - K\tau^{\sigma}\, x \quad (2)$$

where τ is the time a given rock particle has spent within the regolith, and $K\tau^{\sigma}$ represents the dissolution rate constant, which depends on the local climate, exposure time (τ), and an empirical exponent (σ). The evolution of exposure time τ itself is tracked as:

$$\frac{\partial \tau}{\partial t} = -P_r \left(\frac{\partial \tau}{\partial z}\right) + 1 \quad (3)$$

The net weathering rate for the entire regolith column (W, in m/yr) is the integral of the chemical dissolution term over the full regolith thickness:

$$W = \int_0^h K\tau^{\sigma}\, x\, dz \quad (4)$$

where $z = 0$ is at the base of regolith or the surface of bedrock.

2.1.2 Parameterization of Model Components

The key rates in the model (P_r, E, and K) are parameterized as functions of environmental conditions. The production rate (P_r) is modeled as the product of an "optimal" production rate P_0 and a soil-production function $f(h)$ that describes how production decreases with increasing regolith thickness:

$$P_r = P_0\, f(h) \quad (5)$$

https://doi.org/10.5194/egusphere-2025-5624
Preprint. Discussion started: 26 January 2026

where the optimal rate P_0 (which occurs on bare bedrock) is dependent on runoff (q; unit: m/yr) and temperature (T; unit: K), following an Arrhenius relationship:

$$P_0 = k_{rp}\, q\, e^{\left[\left(\frac{E_a}{R}\right)\left(\frac{1}{T_0}-\frac{1}{T}\right)\right]} \tag{6}$$

The soil-production function $f(h)$ takes an exponential form, where d_0 is a reference regolith thickness (m):

$$f(h) = e^{-\frac{h}{d_0}} \tag{7}$$

In the original GM09 model, the physical erosion rate is parameterized using the Stream Power Incision Model (SPIM):

$$E = k_e q^m S^n \tag{8}$$

where k_e is a proportionality constant, S is the local slope (m/m), and m and n are exponents (typically 0.5 and 1). This SPIM formulation (Eq. 8) is the specific component that our new data-driven model replaces, as it is the primary source of the model's systematic biases.

The dependence of the chemical dissolution rate constant on climate is captured by an empirical function that includes the effects of both runoff and temperature:

$$K = k_d(1 - e^{-k_w\, q})\, e^{\left[\left(\frac{E_a}{R}\right)\left(\frac{1}{T_0}-\frac{1}{T}\right)\right]} \tag{9}$$

where k_d and k_w are empirical proportionality constants.

2.1.3 The Steady-State Solution

While GM09 is a transient model, for long-term geological applications it is typically run to a steady-state solution where the regolith thickness is constant ($dh/dt = 0$). This implies that the regolith production rate equals the erosion rate ($P_r = E$). Under this assumption, the complex set of differential equations can be solved analytically. The weathering flux W simplifies to an expression:

$$W = E\left(x|_{z=0} - x|_{z=0} e^{\frac{-k_d\left(1-e^{-k_w\, q}\right) e^{\left[\left(\frac{E_a}{R}\right)\left(\frac{1}{T_0}-\frac{1}{T}\right)\right]}}{\sigma+1}\left(\frac{h}{E}\right)^{\sigma+1}}\right) \tag{10}$$

This steady-state solution (Eq. 10) is central to our study. It explicitly demonstrates that the total weathering flux is the direct product of the physical erosion rate (E) and the total fraction of material that is chemically weathered. This highlights the

https://doi.org/10.5194/egusphere-2025-5624
Preprint. Discussion started: 26 January 2026

paramount importance of accurately estimating E. An incorrect E will propagate directly into an incorrect W, which is precisely the problem we aim to solve.

2.1.4 Data for the Weathering Model

According to Equation (10), apart from the erosion module, weathering flux is also dependent on temperature and runoff. Mean annual temperature (T; K) is derived from CRU TS version 4.03 (Harris et al., 2014), while runoff (R; m/yr) is obtained from the Geophysical Fluid Dynamics Laboratory (GFDL) CM2.0 employed in Park et al. (2020). Zuo et al. (2024) demonstrated that these datasets provide robust performance when applied to silicate weathering models. Note that R is exactly the same as RUNOFF in the erosion module developed by Zhao et al. (2026), while T is the same as MAT in the erosion module but transformed to unit of kelvin.

Moreover, The Ca and Mg cation concentrations (x) depend on the type of rocks. Lithology is from the Global Lithologic Map (GLiM) (Hartmann and Moosdorf, 2012), which provides 16 categorical rock types. We classified the rocks into six groups, following the approach of Park et al. (2020) and Zuo et al. (2024) (see Table S2). The Ca and Mg cation concentrations for each rock type can be obtained from the EarthChem database (http://portal.earthchem.org/, last accessed 23 May 2024). Sedimentary and metamorphic rocks, however, exhibit properties that strongly depend on their protoliths, introducing significant uncertainty into the estimation of silicate weathering fluxes. To address this, Park20 treated the cation concentrations of these two rock categories as adjustable parameters in their model, and the same strategy is applied in this study.

2.2 Development of the New Data-Driven Erosion Model

To address the limitations of the physically simplified SPIM model (Eq. 8), we developed a new global erosion model using a data-driven, machine learning approach as in Zhao et al. (2026). A key difference between the model here and that in Zhao et al. (2026) is the spatial resolution; the latter was trained with data of resolution ~1 km and can output erosion rate at the same resolution, while the former is aiming at a resolution of 0.5°×0.5°. The decrease in resolution is based on the consideration that any model intended for paleo-applications must perform reliably with lower-resolution inputs, and the silicate weathering model described above is widely used in deep-time climate evolution (Mills et al., 2021; Park et al., 2020). For example, the

https://doi.org/10.5194/egusphere-2025-5624
Preprint. Discussion started: 26 January 2026

paleo-digital elevation map (paleo-DEM) normally has a resolution of 0.5°×0.5° or 1°×1° (Scotese, 2021), and the paleo climate data has a resolution of 1°×1° (Li et al., 2022) or lower (Donnadieu et al., 2006; Valdes et al., 2021). Another important difference is that less predictors were used here than in Zhao et al. (2026), as will be described in detail in the subsection 2.2.2. It is unclear whether the model trained with high-resolution data in Zhao et al. (2026) can be fed with low-resolution data (for predictor variables; see below) and output reasonably good low-resolution erosion rate (target variable; also see below). To ensure the consistency between model fitting process and erosion rate predictions, as outlined by Larsen et al. (Larsen et al., 2014) and Willenbring et al. (Willenbring et al., 2014), we use data of 0.5°×0.5° resolution to calculate the basin average environmental predictor values, and use the exactly same map to provide a global prediction. Although basin-average topography is strongly controlled by the spatial resolution (Larsen et al., 2014), tests in latter sections reveal that MErSiM based on a coarse-resolution DEM yielded comparable performance in predicting global pattern of erosion rate to that based on high-resolution DEM.

2.2.1 Target Variable: Basin-Averaged Denudation Rates

Our observational "ground truth" for erosion is derived from the OCTOPUS database (Codilean et al., 2018), which compiles ^{10}Be and other cosmogenic radionuclide (CRN) measurements from fluvial sediments (see Fig. 2 for data distribution and Supplemental material Section 1.1 for technical details). We utilized the global dataset of ~4,100 basin-wide denudation rates (variable name is EBE_MMKYR, in mm/kyr) calculated from ^{10}Be data using the CAIRN program (Mudd et al., 2016), assuming a standard rock density of 2650 kg/m^3.

We used the base-10 logarithm of the denudation rate as the target variable for machine learning. This transformation serves three purposes. First, it converts the highly right-skewed distribution of denudation rates into a more normal distribution, which is better suited for most regression algorithms (see Fig. S1). Second, it minimizes the influence of extreme outliers, enhancing model robustness.

2.2.2 Predictor Variables

The selection of predictor variables/features was guided by established geomorphic principles (Fig. 3). Because the OCTOPUS denudation rates are basin-averaged, all predictor variables were processed to represent basin-wide mean values. The sources,

https://doi.org/10.5194/egusphere-2025-5624
Preprint. Discussion started: 26 January 2026

coverage extent and time window of these variables finally selected are provided in Table S1 and their spatial distribution are shown in Fig. S2.

Basin-mean slope (SLOPE; m/km) and elevation (ELEV; m) are calculated from the 0.5° × 0.5° topography map from Park20 directly, whose topography was from the Shuttle Radar Topography Mission (Farr et al., 2007). When the global erosion rates are calculated on grids, we also take the slope and elevation data from Park20 directly. This data is used so that the silicate weathering fluxes calculated can be compared to those in Park20.

Present-day mean annual temperature (MAT; °C) is from CRU TS v.4.03 (Harris et al., 2014) and runoff (RUNOFF; m/yr) is from the "Yves" dataset from Geophysical Fluid Dynamics Laboratory (GFDL) CM2.0 as used in Park et al. (2020), which were shown by Zuo et al. (2024) to yield strong performance in weathering models. Precipitation of the wettest month (PWET; mm) is from WorldClim 2 (Fick and Hijmans, 2017), and is proved to be one of the most important climatic variables that determines the erosion rate in the detachment-limited regime (Zhao et al., 2026). Leaf Area Index (LAI, unitless) is from NCAR, derived from integrated land observations (Lawrence and Chase, 2007). Lithology (ROCK, unitless) is from the Global Lithologic Map (GLiM) (Hartmann and Moosdorf, 2012), which provides 16 categorical rock types (see Table S2).

To obtain basin averages from the gridded climate, vegetation, and lithology data, we performed a spatial intersection using QGIS (a geographic information system software) so that each basin may be composed of partial grid cells. The value for each basin was calculated via area-weighted averaging for continuous variables (temperature, precipitation, runoff, LAI). For the categorical lithology variable, ROCK, we assigned a dominant rock type to a basin only if a single type covered >70% of its area; basins with more mixed lithologies were excluded to reduce ambiguity. After this filtering, our final dataset for training comprised 3,721 valid samples, each with seven predictor variables: SLOPE, ELEV, MAT, PWET, RUNOFF, LAI, and ROCK.

We also tested the inclusion of peak ground acceleration (PGA; m/s^2), which is an indicator of local tectonic activities. However, as it provided only a marginal improvement in model performance ($\Delta R^2 \approx 0.017$) and is difficult to reconstruct for geological history, it is excluded from the final model. Mean Diurnal Range (MDR; °C) is also excluded in this model because of the limited reconstruction ability in paleoclimate. Hence, another difference between the model here and that in Zhao et al.

https://doi.org/10.5194/egusphere-2025-5624
Preprint. Discussion started: 26 January 2026

(2026) is that less predictors are used herein. Vegetation is represented using LAI rather than Normalized Difference Vegetation Index (NDVI) and the Enhanced Vegetation Index (EVI), because it is a more common output from earth system models. We also tested the effect of other climatic variables that were used in the model of Zhao et al. (2026), such as mean annual precipitation (MAP; mm/yr), seasonality of temperature (TSEASON; °C; the standard deviation of monthly temperature) and precipitation (PSEASON; defined as the ratio of the standard deviation of monthly mean to the annual mean precipitation rate, in unit %), temperature of the coldest month (TMIN; °C), all collected from WorldCLim 2 (Fick and Hijmans, 2017). However, adding these variables did not improve but deteriorate the performance on the calculation of both erosion rates and weathering flux when using 0.5°×0.5° data, especially the latter (Table 1), and thus not considered in this study.

2.2.3 Machine Learning Algorithm Selection and Training

We compared several supervised regression algorithms, including linear models, decision trees, gradient boosting, and Random Forest. While decision trees offer excellent interpretability, Random Forest consistently yielded the highest predictive accuracy (see Supplemental material section 1.2 and Fig. S3 for details). The Random Forest (RF) algorithm (Breiman, 2001) is an ensemble model that builds a multitude of decision trees and aggregates their predictions. It is particularly well-suited for environmental data due to its ability to handle complex non-linearities and its robustness to multicollinearity (e.g., the correlation between latitude, elevation, and temperature).

The dataset was randomly split into a training set (80%) and a testing set (20%). We performed a grid search with 10-fold cross-validation on the training set to identify the optimal combination of hyperparameters. The search grid included: ntree (number of trees): [300, 500]; mtry (number of variables to sample at each split): [2, 5]; nodesize (minimum samples in a terminal node): [1, 5]; maxdepth (maximum tree depth): [10, 30]. The optimal combination that minimized RMSE was found to be: ntree=500, mtry=2, nodesize=1, maxdepth=30. The final RF model was trained on the full training set using these parameters and evaluated on the unseen testing set.

To understand the drivers learned by the model, the importance of each predictor or feature variable is ranked based on the TreeSHAP method. TreeSHAP is a variant for tree-based machine learning models of SHapley Additive exPlanations (SHAP; (Lundberg and Lee, 2017), which is based on coalitional game theory (Shapley, 1953). TreeSHAP scores

https://doi.org/10.5194/egusphere-2025-5624
Preprint. Discussion started: 26 January 2026

(positive/negative or null) of each feature are the changes in the expected model prediction due to that feature. Specifically, it is the average change in the model's output when this feature is varied over all possible values, while keeping all other features constant.

2.3 Model Coupling and Evaluation Setup

2.3.1 Integration of the Machine Learning-based Erosion Model into GM09

The trained RF model was used to predict a global map of erosion rates (E_{RF}) at 0.5° × 0.5° resolution. This data-driven erosion map was then used as the direct input for the erosion rate E in the GM09 weathering model framework. We refer to the original model using the SPIM erosion law as GM09-SPIM, and our improved version with the new erosion map as MErSiM.

2.3.2 Evaluation Framework

To provide a robust and fair comparison, both the GM09-SPIM and MErSiM models were run using identical boundary conditions, including the same GLiM lithology map and climate forcing fields. The model outputs, generated at a 0.5° × 0.5° resolution were evaluated against established observational datasets.

Our primary validation dataset for silicate weathering is the widely-used compilation by Gaillardet et al. (1999). This dataset provides observation-based estimates of silicate-derived Ca^{2+} and Mg^{2+} fluxes for 52 of the world's largest river basins. These fluxes are inferred from river water chemistry using an inverse method to deconvolve sources (atmospheric, carbonate, silicate, anthropogenic), which is particularly effective for large, lithologically complex catchments.

Zuo et al. (2024) noted a significant discrepancy in the Amazon basin between the weathering flux reported by Gaillardet et al. (1999) (~0.02 mol m^{-2} yr^{-1}) and that from the HYBAM (Hydrogeochemistry of the Amazon Basin) observatory (~0.07 mol m^{-2} yr^{-1}), which consists of 32 smaller, well-monitored sub-catchments (Moquet et al., 2011, 2016). Instructed by the result of Zuo et al. (2024), we validate MErSiM using a combined dataset where the Amazon basin data from Gaillardet is replaced by the HYBAM data. Following community practice (Park et al., 2020; Zuo et al., 2024), we focus our main analysis on the 81 non-overlapping major basins from this compilation.

We assessed the agreement between modeled and observed fluxes for each basin using the coefficient of determination (R^2). Following Zuo et al. (2024), we consider both the standard R^2 (calculated on direct values) and the R^2 calculated on $\log_{10}$-

https://doi.org/10.5194/egusphere-2025-5624
Preprint. Discussion started: 26 January 2026

transformed values (R^2_{log}). The former is sensitive to biases in total flux, while the latter better reflects the model's ability to capture the correct order of magnitude across diverse basins. We also use $R^2 + R^2_{log}$ as the final evaluating metric as Zuo et al. (2024). Note that $R^2 + R^2_{log}$ was also maximized for GM09-SPIM by searching the model parameter space (see Table 2 for the parameters that are searched), in addition to the model parameters previously fitted by (Park et al., 2020). By using this comprehensive evaluation framework, which includes multiple observational benchmarks, we can rigorously quantify not only if our new model (MErSiM) is better, but specifically how and where it improves upon the reference model GM09-SPIM.

To ensure that our calibrated parameter set represents a robust optimal solution rather than an arbitrary point in a poorly constrained parameter space, we performed a comprehensive sensitivity analysis. Fig. S4 visualizes slices of the high-dimensional parameter space, illustrating how model performance (quantified by the $R^2 + R^2_{log}$ metric) varies with changes in key parameters. The results demonstrate that our optimization has converged on a well-defined and constrained solution. Across the plots for the primary kinetic parameters (σ, k_w, k_{rp}, Fig. S4a-c), a distinct high-performance region (the bright yellow "sweet spot") emerges, centered around our selected optimal values (indicated by the red boxes). The plots for lithological parameters (Fig. S4d-e) reveal that while the model performance is highly sensitive to the choice of k_d, it is relatively insensitive to a wide range of cation concentrations for both metamorphic and sedimentary rocks, as long as k_d is within its optimal range.

2.4 Sensitivity of Global Weathering Rate to Climate Change

The climate sensitivity of global silicate weathering was tested for both cooling and warming, as was done in Zuo et al. (2024). For cold climates, the Last Glacial Maximum (LGM) was selected, using datasets from Zhang et al. (2022). MAT (the same as T in Equation. (9) and (10) for calculating weathering flux), RUNOFF (also q in Equation (9) and (10)), LAI, and PWET are averaged over year 3971–4000 of the model output. For warm climates, the abrupt 4×CO_2 experiment conducted with CESM2 (Danabasoglu et al., 2020) was used, with data obtained from the CMIP6 archive (https://esgf-metagrid.cloud.dkrz.de/, last access: 10 September 2025). MAT, RUNOFF, LAI and PWET were also from the last 30 years of the simulation results. In both cases, lithology, slope, and elevation were kept the same as the present.

https://doi.org/10.5194/egusphere-2025-5624
Preprint. Discussion started: 26 January 2026

3 Results and Discussion

This section presents the main findings of our study. We first evaluate the performance of the new data-driven erosion model against existing models, and then examine the global erosion patterns predicted by MErSiM and compare them to the SPIM employed in the original GM09. Next, we analyse the internal workings of the machine learning model to understand the physical relationships it has learned. Finally, and most importantly, we present the results of the silicate weathering model (MErSiM), demonstrating its ability to resolve the systematic biases present in the original GM09-SPIM framework.

3.1 Performance of the New Data-Driven Erosion Model

The foundational hypothesis of this study is that the inaccuracies in global silicate weathering models stem primarily from a poorly constrained erosion module. Therefore, the first critical test is to demonstrate that our new erosion model, developed using a Random Forest (RF) algorithm trained on the OCTOPUS ^{10}Be database, provides a better representation of real-world denudation rates compared to existing approaches.

Figure 4 presents a direct, quantitative comparison of the predictive power of three different erosion models. In each panel, the x-axis represents the "ground truth" basin-averaged denudation rates derived from the OCTOPUS database, while the y-axis shows the corresponding rates predicted by a given model. All the feature data of river basins input into the three models are the same, only methods of calculating erosion rates are different. Fig. 4a displays the performance of our newly developed Random Forest model. The data points form a tight, well-defined cluster centered directly on the 1:1 line across the entire range of denudation rates, from less than 1 mm/kyr in stable, low-relief settings to over 1000 mm/kyr in rapidly eroding, tectonically active regions. The calculated R^2_{log} value is 0.94, signifying that model can explain more than 90% of the variance in the global ^{10}Be-derived denudation rate database. This high degree of accuracy and low level of bias demonstrates the exceptional capability of the RF algorithm to learn the complex, non-linear relationships governing erosion from the provided multi-variate environmental data.

Note that Fig. 4a looks similar to Fig. 7b in Zhao et al. (2026) but there are two major differences between the model there and RF model here. The first difference is that the model here has 7 predictors, 7 less than the model in Zhao et al. (2026). The second difference is that the model here is trained and validated with feature variables calculated from coarse-resolution (0.5° × 0.5°) data, compared to their 1 km × 1 km resolution.

https://doi.org/10.5194/egusphere-2025-5624
Preprint. Discussion started: 26 January 2026

Crucially, the performance of MErSiM significantly surpasses that of existing models. The original Stream Power Incision Model (SPIM) used in Park20 (Equation (8) above with $k_e = 0.0029110, m = 0.5, n = 1$) shows a weak correlation with observations, explaining only ~20% of the variance (R^2_{log} = 0.23, Fig. 4c). The data points are not only diffuse, but also have significant systematic bias; they overestimate the actual denudation rates at the lower end and underestimate at the higher end. The improved model by Zuo et al. (2024), which incorporates a dependency on Leaf Area Index (LAI), offers a modest improvement but still only achieves an R^2_{log} of 0.38 (Fig. 4d). This result quantitatively confirms the central premise of our work: the simplified, physically-based SPIM, while conceptually useful, has its apparent weakness in predicting basin-scale denudation rates at the global scale. Its limited explanatory power could be the root cause of the problems in the silicate weathering model.

3.2 Global Erosion Patterns and Comparison with SPIM

Having established the statistical excellence of the RF erosion model, we next examine its spatial predictions on a global scale and compare them to the patterns generated by the SPIM and model revised by (Zuo et al., 2024). This comparison is crucial for understanding why MErSiM ultimately corrects the weathering fluxes, by diagnosing the specific geographic regions where the old and new models diverge most significantly.

Fig. 5 presents three global maps at a 0.5° × 0.5° resolution. The spatial pattern predicted by our random forest model (E_{RF}; Fig. 5a) are geomorphologically intuitive and consistent with modern tectonic and climatic knowledge. The highest rates of erosion (in red, exceeding 200 mm/kyr) are sharply localized to the world's major active orogenic belts: the Andes in South America, the Himalayan-Tibetan Plateau complex in Asia, the Alps in Europe, and the North American Cordillera. Conversely, vast continental interiors and stable cratons, such as central Australia, Siberia, the Canadian Shield, and large parts of Africa, are correctly depicted with very low erosion rates (in blue). This map represents a new data-constrained view of the Earth's long-term erosional engine.

Figure 5c shows the corresponding global erosion map calculated using the SPIM formulation (E_{SPIM}) as in Park20. While the SPIM also captures the high erosion rates in major mountain belts, a critical and fundamental difference is immediately apparent in the tropics. The SPIM predicts extremely high erosion rates across vast, low-lying areas of the humid tropics, most notably the Amazon Basin, the Congo Basin, and the archipelagos of Southeast Asia. These regions are depicted in shades of

https://doi.org/10.5194/egusphere-2025-5624
Preprint. Discussion started: 26 January 2026

red and orange, suggesting erosion rates comparable to those in mountainous regions. This artifact is a direct consequence of the SPIM's mathematical form (Eq. 8), where the erosion rate is a power-law function of runoff (q). In these regions, extremely high annual runoff overwhelms the effect of the very low topographic slopes, leading to a probably physically unrealistic prediction of intense erosion.

Fig. 5d crystallizes this divergence by showing the difference between the two models (RF minus SPIM). The map is overwhelmingly dominated by shades of blue and deep blue in tropical regions. This signifies that our RF model predicts substantially lower erosion rates—in many areas, more than 100 mm/kyr lower—than the SPIM throughout these regions. This is the geographic fingerprint of the correction MErSiM provides. It has learned from the ^{10}Be data that high runoff in low-slope environments does not necessarily translate to high erosion rates, a crucial real-world constraint that the simplified physics of the SPIM fails to capture. The systematic over-prediction of tropical erosion by the SPIM is the direct mechanism for the subsequent over-prediction of tropical silicate weathering, a problem MErSiM aims to solve.

Beyond this primary correction in the tropics, the difference map (Fig. 5d) reveals another important, albeit more subtle, pattern. Patches of blue are also visible along the crests of the highest mountain ranges, such as the Himalayas and the Andes. This indicates that our RF model also predicts lower erosion rates than the SPIM in these extremely steep landscapes. This result is consistent with a well-documented phenomenon in geomorphology where, above a certain slope threshold (often cited around ~30°, calculated using 90 m DEM), erosion rates tend to plateau or even decrease (Ouimet et al., 2009). This is often attributed to a shift from transport-limited to detachment-limited denudation, where the rate of soil and regolith production cannot keep pace with the transport capacity, leading to extensive bare bedrock exposure which is harder to erode (Binnie et al., 2007; Ouimet et al., 2009). The SPIM, with its power-law dependence on slope, cannot capture this saturation effect. Our data-driven RF model, however, has learned this more complex, non-linear relationship from the ^{10}Be observations, as shown in detail in Zhao et al. (2026), further enhancing its physical realism compared to the simplified model. This demonstrates that the improvements offered by MErSiM are not confined to the tropics but extend to capturing more nuanced geomorphic processes in the world's most dynamic landscapes. Another notable difference is an increase in erosion rate emerged from Random Forest model's predictions than SPIM in high-latitude cold regions (above 45°N) of Northern Hemisphere (Fig. 5d).

https://doi.org/10.5194/egusphere-2025-5624
Preprint. Discussion started: 26 January 2026

This is mainly due to the model's identification of intense frost-cracking that set the pace of landscape evolution in cold climates, which we will analyse in detail in the next section.

Zuo et al. (2024) also used the SPIM model to calculate erosion rate but lowered its value by approximately an order of magnitude wherever the LAI is greater than 2 (Fig. 5b). This was done to reduce the discrepancy between the simulated and observed silicate weathering fluxes especially in tropical regions. Fig. 5f shows how much and where the erosion rate was changed relative to the SPIM model. It can be seen that the crude approach adopted by Zuo et al. (2024) lowers the erosion rates over south east Asia islands and Amazon basins, but gives a systematically larger prediction of erosion rates in the mountainous regions (Fig. 5f). This is mainly because they applied the scaling method to keep the global erosion flux constant at 20 Gt/yr, which is the same as SPIM. Reductions of erosion rates in tropical regions therefore demand an increase in other regions, where those eroded the strongest increase the most after scaling. However, as discussed above, the erosion rates in these steep regions have already been overestimated in SPIM model. This bias is even larger in Zuo et al.'s revised erosion model (Fig. 5e).

3.3 Interpretation of the Machine Learning Model: Feature Importance and Dependencies

3.3.1 Dominance of Topography and Climate

A common criticism of machine learning models is that they can be "black boxes," providing accurate predictions without revealing the underlying physical mechanisms (Breiman, 2001). To address this and build confidence in MErSiM's physical realism, we employed SHAP (SHapley Additive exPlanations) analysis. SHAP is a state-of-the-art method that assigns each feature an importance value for every individual prediction, allowing us to move beyond general rankings and understand the nuanced, non-linear effects of each environmental driver. We also calculate the spearman correlation of erosion rates and each feature. Fig. 6 and Fig. 7 provides insights into which environmental factors the model found to be most important and the nature of their relationships with erosion.

Fig. 6a displays the global feature importance, calculated as the mean absolute SHAP value across all training samples. SLOPE emerges as the unequivocally dominant predictor, with a mean SHAP value of 0.6, nearly double that of the next most important feature. This finding is geomorphologically reassuring, as it aligns with geomorphic research and first-principles understanding (Milliman and Syvitski, 1992; Portenga and Bierman, 2011; Riebe et al., 2001), and also consistent with

https://doi.org/10.5194/egusphere-2025-5624
Preprint. Discussion started: 26 January 2026

previous data-driven analysis (Portenga and Bierman, 2011). It confirms that our data-driven model has independently learned that topography is the master variable controlling the pace of erosion at a global scale.

Following slope, a group of climatic variables—MAT (Mean Annual Temperature) and RUNOFF—exhibit significant and comparable importance (SHAP values of 0.39 and 0.34, respectively). This highlights that after the primary topographic driver, the model relies heavily on climatic conditions to refine its predictions. Note that the influence of RUNOFF is secondary after SLOPE and even MAT, a contrast to the SPIM, where runoff is a dominant, first-order driver. The RF model has learned that high runoff only leads to high erosion when other conditions, primarily steep slopes, are met (see below).

LAI (Leaf Area Index) follows as a moderately important factor, underscoring the role of vegetation in modulating erosional processes. PWET (Precipitation of the Wettest Month) and ELEV (Elevation) show lower, yet still relevant, importance, while ROCK (Lithology) has the least impact, suggesting that at a global scale, broad rock types are less predictive than the dynamic interplay of topography and climate.

This order of importance, where slope ranks the first with significantly higher SHAP value, then following climatic variables with similar importance, and rock type ranks the last, is well consistent with that in Zhao et al. (2026), even when they have 14 predictor features included.

The Spearman correlation plot (Fig. 6b) shows strong positive correlations between erosion rate and SLOPE, and moderate positive correlations with ELEV and RUNOFF, indicating that steeper, higher, and wetter environments generally erode faster. MAT displays a negative correlation with erosion rate.

To move beyond general feature rankings and understand the nonlinear effects of each predictor, we utilize SHAP dependence plots (Fig. 7). Each point on a SHAP dependence plot represents a single sample (i.e., a river basin) from our dataset. The horizontal axis indicates the actual value of the feature for that sample, while the vertical axis shows its corresponding SHAP value. The SHAP value itself quantifies the magnitude and direction of a feature's contribution to a single prediction, relative to the baseline (mean) prediction across all samples. Its units are the same as the model's output—in our case, logarithmic erosion rate. Here, our baseline is 4.4 (equivalent to an erosion rate of ~78 mm/kyr). This is the model's best prediction without any specific information. If we provide the model with the specific features of predictors: for instance, one of river basins in Dadu, SLOPE = 13.6°, MAT = 6.7°C, RUNOFF = 0.75 m/yr, and so on. The model processes these inputs and yields a final

https://doi.org/10.5194/egusphere-2025-5624
Preprint. Discussion started: 26 January 2026

prediction, 6.1 (equivalent to ~438 mm/kyr). The SHAP values explain precisely how the model arrived at this prediction by decomposing the difference between the final prediction (6.1) and the baseline (4.4). Each feature is assigned a SHAP value representing its individual contribution:

$$Baseline + \Sigma(SHAP\ values\ for\ all\ features) = Final\ Prediction$$

In this case, $SHAP_{SLOPE} = 0.91, SHAP_{MAT} = 0.14, SHAP_{RUNOFF} = 0.34, SHAP_{LAI} = 0.28, SHAP_{PWET} = 0.03, SHAP_{ELEV} = -0.01, SHAP_{ROCK} = 0.03$, then:

$$4.4 + (0.91 + 0.14 + 0.34 + 0.28 + 0.03 - 0.01) = 4.4 + 1.7 = 6.1$$

The resulting distribution of points thus reveals the overall relationship—be it linear, non-linear, monotonic, or more complex—between a feature's magnitude and its impact on the model's output.

The SHAP value of SLOPE (Fig. 7a) is negative for gentle slopes (< ~3°), indicating that flat landscapes actively suppress erosion predictions. Above this threshold, the SHAP value increases steeply and almost linearly up to about 10-15°, after which the effect begins to saturate. This saturation is physically realistic and consistent with a shift from transport-limited to detachment-limited regimes in the steepest landscapes, a nuance that simple power-law models like SPIM cannot capture (Binnie et al., 2007; Ouimet et al., 2009).

For MAT (Fig. 7b), the model has learned a complex relationship. When MAT is below ~10°C, SHAP values are positive and peak at ~0°C (i.e., cold temperatures push erosion predictions higher and this effect is the strongest around 0°C). This is consistent with the "frost-cracking window" hypothesis, which posits that erosion is maximized not in the absolute coldest environments, but in those that experience frequent oscillations across the 0°C threshold (Anderson and Anderson, 2010; Delunel et al., 2010). These freeze-thaw cycles generate substantial mechanical stress within bedrock fractures, leading to efficient rock breakdown and the production of a large volume of transportable sediment, even in the absence of steep topographic gradients (Hales and Roering, 2007). Above ~10°C, warmer temperatures are associated with lower erosion predictions, and this lowering effect remains the strongest around 20-25°C. This negative trend in warmer climates likely captures multiple effects, including the stabilization of landscapes by tropical leached soil (deeply weathered, erosion-resistant regoliths) as noticed before by Zuo et al. (2024).

https://doi.org/10.5194/egusphere-2025-5624
Preprint. Discussion started: 26 January 2026

The effect of RUNOFF (Fig. 7c) is highly non-linear and exhibits a clear optimal peak. Erosion predictions increase with runoff up to about 1.7 m/yr, after which higher runoff values lead to a decrease in predicted erosion. It suggests the model has learned that moderate runoff in transport-capable landscapes is the most effective to activate hydrological erosion (Carretier et al., 2013; DiBiase and Whipple, 2011). However, the decrease of variability in discharge with the increase of runoff under wetter conditions (e.g., > 2 m/yr) would result in a suppressed net impact on erosion (DiBiase and Whipple, 2011; Lague, 2014; Perron, 2017). The asymmetric hump-shaped relationship has also been reported and discussed in detail in the statistical analysis of Zhao et al. (2026). This data-driven insight directly refutes the monotonic, power-law assumption of the SPIM.

The SHAP plot for LAI (Fig. 7d) reveals its dual role. At very low LAI values (< ~0.5), it has a slight positive effect, likely reflecting arid or semi-arid environments where sparse vegetation is insufficient to stabilize mobile sediment. As LAI increases from ~0.5 to ~2.5, it exerts a strong negative influence on erosion, capturing the well-established stabilizing effect of root systems and canopy cover (Mishra et al., 2019; Prosser et al., 1995). Interestingly, at very high LAI values (> 3), the negative impact lessens. This could reflect the fact that the most densely vegetated regions on Earth are often flat, stable cratons where erosion is already intrinsically low, so additional vegetation has a diminishing marginal effect (Heimsath et al., 1997).

The SHAP dependence plot of the least three variables (PWET, ELEV and ROCK) show their less significant effects on erosion rates and more ambiguous trends (Fig. S5), so the analyses of their effects are only briefly described in the supplementary material.

3.3.2 Dominant Environmental Factors Revealed by the Decision Tree

A representative decision tree from the Random Forest ensemble (Fig. 8) offers a powerful visualization of the complex hierarchical relationships learned by the model. The tree structure reveals that the importance of different variables is conditional and depends on the specific environmental context.

The very first split at the top of the tree is based on SLOPE, with a threshold of 2.5° (calculated from DEM with 0.5° × 0.5°). This immediately separates the world into low-relief and high-relief domains, indicating that the fundamental drivers of erosion differ profoundly between these two settings.

In the flattest parts of the world (SLOPE < 2.5°), the model turns to MAT. This is also seen in the analysis of Zhao et al. (2026) in their model with more predictors. In these areas, the effect of river incision is weaker and the rate of erosion may be more

https://doi.org/10.5194/egusphere-2025-5624
Preprint. Discussion started: 26 January 2026

strongly influenced by the rate of chemical decomposition or by freeze-thaw cycle (Anderson and Anderson, 2010; Delunel et al., 2010; White and Blum, 1995).

LAI became an important predictor as the slope steepened (2.5° ≤ SLOPE < 6.3°), and the data-driven model calculated an LAI threshold of 2. This value is exactly the same as the threshold used for the modification of the erosion model in Zuo et al (2024), where the value was obtained by human judgement. Vegetation can prevent erosion by increasing surface roughness, disrupting overland water flow, and stabilizing the soil through the root system (Mishra et al., 2019; Prosser et al., 1995). The overall weak negative correlation between LAI and erosion rates and the branches in the decision tree suggest that vegetation primarily serves to reduce erosion.

In steep landscapes (SLOPE >= 6.3°), the model identifies RUNOFF as the next most important variable, with thresholds of 0.27 m/yr (Fig. 8). This suggests that in very steep terrain, there is an abundant supply of material, and the rate of regolith detachment becomes limited by the availability of water to move it (DiBiase and Whipple, 2011; Snyder et al., 2003; Tucker, 2004).

3.4 Impact on the Silicate Weathering Model

Zuo et al. (2024) highlighted a critical trade-off in the original GM09 model: it was impossible to find a single set of parameters that could simultaneously match the global total flux and the spatial distribution of weathering across watersheds. Fig. 9 visualizes this problem and demonstrates how our new model resolves it.

The Fig. plots the model performance (R^2 values) as a function of the resulting global weathering flux for all possible parameter combinations (the parameters and their ranges are listed in Table 2). The vertical grey bar indicates the target range for the global flux based on observations. Fig. 9a, representing the original GM09-SPIM model, clearly illustrates the trade-off. To achieve the highest R^2_{log} value (the peak of the yellow curve), which measures the fit to the spatial pattern, the model must produce a global total flux (the x-axis value corresponding to the peak) far to the right of the observed range, giving an overestimation. Conversely, if one forces the model to match the observed global flux (where the curves intersect the grey bar), then the R^2_{log} value is low, indicating a poor fit to the spatial pattern. Optimizing the parameter set by using R^2 metric as a target is even worse (red dots and curve in Fig. 9a). Optimizing the parameter set by using the sum of R^2 and R^2_{log} guarantees a reasonable global total flux (blue dots and curve in Fig. 9a) but gives an unsatisfying spatial pattern; the sum of R^2 and R^2_{log}

https://doi.org/10.5194/egusphere-2025-5624
Preprint. Discussion started: 26 January 2026

peaks at only 0.55. This shows that the model cannot be both "right in total" and "right in pattern", which is why Zuo et al. (2024) chose to adjust the erosion rate in a partially subjective way in addition.

Fig. 9b, showing the performance of our MErSiM model, demonstrates a resolution of this issue. The peaks of all three metric curves (R^2, R^2_{log}, and $R^2 + R^2_{log}$) are now located squarely within the grey observational band. Specifically, the highest value of $R^2 + R^2_{log}$ reaches 0.86. This signifies that the MErSiM model achieves its optimal performance—its best possible fit to the watershed-scale data—at a global flux value that is already consistent with observations. The fundamental conflict between matching the total and matching the pattern has been eliminated. This result indicates that our MErSiM is not just a better-tuned model, but a more physically coherent representation of the global silicate weathering system. By providing an accurate, data-constrained erosion field, we allow the weathering model's chemical kinetics to operate within a realistic physical context, leading to a robust and reliable simulation framework.

The basin-wise improvement of weathering fluxes by the MErSiM model relative to the GM09-SPIM model is demonstrated in Fig. 10, where the difference between the modelled and observational values for 81 major river basins (see subsection 2.3.2) are shown. The GM09-SPIM model shows large positive error within the tropical regions, especially over South America and Africa (Fig. 10a-b), with errors often exceeding 0.7 x 10^{11} mol/yr. The total weathering flux predicted by this model is ~4.5 × 10^{12} mol C yr^{-1}, an ~80% overestimate compared to the observation-based estimate of ~2.5 ± 0.5 × 10^{12} mol C yr^{-1}. In comparison, the tropical overestimate is much less severe in MErSiM model (Fig. 10c-d). The errors are also much more balanced globally, with a mix of small positive and negative errors distributed across different climatic zones, giving a total weathering flux more align with observations (~3.1 x 10^{12} mol C yr^{-1}).

3.5 Sensitivity of global silicate weathering to climate change

To evaluate how our revisions to the erosion module affect the feedback strength of silicate weathering, we conducted a series of sensitivity experiments using standardized climate forcing scenarios: the Last Glacial Maximum (LGM), the Pre-Industrial (PI), and an abrupt 4×CO_2 experiment. As shown in Table 3, the global mean land surface temperature increases by 8.2 K from LGM to PI, and by a further 14.5 K from PI to the 4×CO_2 scenario. We forced both the original Park20 model and our revised model (hereafter MErSiM) with these climate fields to assess their responses.

https://doi.org/10.5194/egusphere-2025-5624
Preprint. Discussion started: 26 January 2026

3.5.1 Reduced Absolute Fluxes and Attenuated Warming Sensitivity

Consistent with our modern-day simulations, the MErSiM model predicts significantly lower absolute global weathering fluxes across all climate cases compared to the Park20 model (Table 3). The PI flux in MErSiM is 3.11×10^{12} mol yr^{-1}, approximately 2/3 of the 4.54×10^{12} mol yr^{-1} predicted by the Park20 model, bringing the weathering fluxes approximately within the range of observation-based estimates (Gaillardet et al., 1999; Moon et al., 2014).

More importantly, our revised model exhibits a markedly different sensitivity to climate change. From LGM to PI, the weathering flux in MErSiM increases by 0.99×10^{12} mol yr^{-1}, a relative increase of 47%. This is comparable to the 46% increase predicted by the Park20 model, suggesting that both models capture a similar weathering response to glacial-interglacial warming (Fig. 11a). However, the response to intense warming in the $4\times CO_2$ scenario diverges dramatically. While the Park20 model predicts a massive increase in weathering of 6.77×10^{12} mol yr^{-1} (a 149% increase from PI), our MErSiM model predicts a much weaker response of only 1.33×10^{12} mol yr^{-1} (a 42% increase, Fig. 11b). This profound attenuation of weathering sensitivity under warm, high-CO_2 conditions is a key finding of our study and points to a shift in the weathering regime captured by our improved erosion module.

3.5.2 Interpretation to the Reduced Sensitivity

The dampened response of MErSiM stems from a combination of a structural change in the model's physics and a corresponding shift in its calibrated chemical parameters.

The primary reason for the reduced sensitivity is the replacement of the simplistic SPIM erosion law with our data-driven, machine learning-based module. The SPIM creates a strong, near-universal positive coupling between runoff and erosion. Consequently, in a $4\times CO_2$ world with enhanced runoff, the Park20 model simulates a widespread, dramatic increase in erosion, continuously supplying fresh material and allowing chemical weathering to accelerate freely with rising temperatures.

Our ML-based erosion model, constrained by ^{10}Be data, imposes a ceiling on erosion rates. It has learned that in many landscapes—particularly those with low-to-moderate slope that constitute the bulk of Earth's land area—erosion is strongly constrained by topography and vegetation, and does not accelerate dramatically with increased runoff alone (Fig. 7a,c). Moreover, erosion rates are overall negatively correlated with mean annual temperatures (Fig. 6b), especially in the flattest areas, where higher temperatures tend to make it more difficult for freeze-thaw cycles to occur and erosion rates to decrease

https://doi.org/10.5194/egusphere-2025-5624
Preprint. Discussion started: 26 January 2026

(see decision tree in Fig. 8). As a result, when faced with the strong warming and hydrological intensification of the 4×CO_2 scenario, the acceleration of erosion due to enhanced runoff is largely offset, or even reversed, by the overall suppression of erosion by elevated temperatures, notably in the higher latitudes beyond 50° (Fig. 11d). Weathering fluxes are limited by the supply of erosion, effectively decoupling weathering from the large increase in chemical weathering potential due to temperature increase.

The second reason is a new kinetic pattern reflected by calibrated parameters. To match modern observational constraints within this erosion framework, MErSiM calibration converged on a set of chemical kinetic parameters that describe a far more "sluggish" weathering system than that of Park20 (Table 2). The most significant changes are (1) a 5-fold decrease in the base dissolution rate constant (k_d) (5e^{-4} vs. 1e^{-4}), lowering the intrinsic speed of chemical reactions; (2) a 5-fold decrease in the runoff sensitivity parameter (k_w) (1.0 vs. 0.2), making chemical weathering less responsive to increases in water availability. (3) a qualitative shift in the weathering time-exponent (σ) from -0.4 to positive -0.1, implying a slower decay of reaction rates as minerals reside in the regolith.

These parameters are not arbitrary. The model has discovered that to explain today's weathering fluxes in a world where erosion is not as dynamic as previously assumed, the chemical processes themselves must be inherently slower and less sensitive. This finding is supported by several lines of evidence and theoretical work. A long-standing challenge in geochemistry is the dramatic discrepancy, often spanning several orders of magnitude, between mineral dissolution rates measured in the laboratory and those observed in the field (White and Brantley, 2003). The 5-fold lower dissolution constant (k_d) value derived from our calibration reflects a large-scale effective rate compared to the rapid rates seen on fresh mineral surfaces under ideal laboratory conditions. This rate is naturally attenuated by processes such as the formation of passivating secondary mineral coatings, the reduction of reactive surface area over time, and the complexities of fluid flow paths within the regolith.

This finding can also be explained by the hydrologic regulation framework of Maher & Chamberlain (2014), which posits that weathering fluxes are governed by the competition between fluid travel time (τ_f) and the time required for reactions to approach equilibrium (τ_{eq}). Our results can be interpreted through the lens of their Damköhler number formulation. The high dissolution constant (k_d) in the Park20 model implies a very short intrinsic equilibrium time (τ_{eq}), suggesting a system that can rapidly approach its "thermodynamic limit." This allows weathering fluxes to scale aggressively with increased runoff,

https://doi.org/10.5194/egusphere-2025-5624
Preprint. Discussion started: 26 January 2026

particularly in high-relief areas. In contrast, the 5-fold lower k_d value and altered kinetic exponent (σ) derived from our calibration describe a system with a much longer intrinsic τ_{eq}. According to Maher & Chamberlain (2014), weathering fluxes plateau and become limited when fluid travel times become short relative to the equilibrium time ($\tau_f < \tau_{eq}$). In a warmer world with a greatly intensified hydrologic cycle, runoff increases, leading to a global decrease in τ_f. For the Park20 model, with its inherently short τ_{eq}, the system relatively remains in a state where $\tau_f > \tau_{eq}$, and weathering fluxes continue to climb even with shorter time for chemical reaction. However, for our revised model, this widespread decrease in τ_f causes vast terrestrial areas to be pushed into the regime where equilibrium could not be fully established. In this state, the system becomes "chemostatic". Solute concentrations decrease as runoff increases, and the overall weathering flux saturates. The lower runoff sensitivity (k_w = 0.2) in our revised model is a direct macro-scale expression of this saturation effect. Our model has learned from the data that, on a global scale, many landscapes already operate closer to this chemostatic boundary than previously assumed. Consequently, under the intense hydrological forcing of a 4×CO_2 world, they cannot deliver a proportionally large increase in weathering flux.

3.6 Scope of Applicability and Model Limitations

MErSiM v1.0 is primarily designed for integration into Earth System Models (ESMs) and geochemical box models to simulate the long-term carbon cycle and climate evolution on geological timescales (10^5 to 10^7 years). The model is specifically optimized for deep-time paleo-applications where boundary conditions (e.g., paleogeography, lithology, and climate fields) are often constrained to coarse resolutions. By operating at a spatial resolution of 0.5°×0.5°, MErSiM strikes a balance between capturing regional heterogeneity in weathering fluxes—such as the high fluxes in orogenic belts —and maintaining computational efficiency for long-term simulations. The model is particularly suitable for investigating the silicate weathering feedback under extreme climate states, such as greenhouse worlds, where it resolves the biases of traditional power-law erosion models.

Despite its improvements, the model has several limitations that users should consider. First, the erosion module is a data-driven Random Forest model trained on modern basin-averaged ^{10}Be denudation rates. While we identified physical drivers (slope, runoff, temperature) consistent with geomorphic principles, the application to deep-time scenarios assumes that the fundamental relationships governing erosion have remained consistent. Caution is advised when applying the model to eras

https://doi.org/10.5194/egusphere-2025-5624
Preprint. Discussion started: 26 January 2026

with fundamentally different surface conditions (e.g., pre-vegetation landscapes in the Precambrian), although the explicit inclusion of LAI as a predictor allows for some sensitivity testing.

Second, the model is trained and validated at a basin-averaged scale using 0.5°×0.5° resolution inputs. It is not intended for local, hillslope-scale geomorphological studies or for capturing short-term transient erosion events (e.g., landslides or individual storms) that are smoothed out in long-term average denudation rates (Larsen and Montgomery, 2012).

Third, while MErSiM incorporates the Global Lithologic Map (GLiM) categories (Hartmann and Moosdorf, 2012), the chemical weathering calculations for complex lithologies (sedimentary and metamorphic rocks) rely on calibrated bulk cation concentrations (Park et al., 2020). This approach neglects the specific mineralogical evolution within sedimentary basins over time, which introduces uncertainty when detailed lithological reconstructions are unavailable.

Last but not least, the current version of MErSiM primarily operates under a steady-state assumption for regolith thickness (where production equals erosion) to derive weathering fluxes efficiently (Gabet and Mudd, 2009). While suitable for long-term carbon cycle modelling, this assumption may limit its applicability in scenarios with extremely rapid tectonic uplift or climatic perturbations where the transient response of the regolith is the primary focus.

4 Conclusions

This study was motivated by a critical and systematic flaw in the state-of-the-art, process-based global silicate weathering model (GM09), which overestimates weathering fluxes in tropical regions and produces a global total flux nearly double the observation-based estimates. We have demonstrated that this discrepancy originates not in the model's chemical kinetics but in its physically oversimplified and poorly constrained erosion submodule. To resolve this, we developed a new global erosion model using a Random Forest algorithm trained on about 4,000 ^{10}Be-derived denudation rates. This data-driven model represents a step-change in predictive power, explaining over 90% of the variance in the observational data and far exceeding the performance of the traditional Stream Power Incision Model (SPIM) and other existing approaches. By integrating this superior erosion module into the GM09 framework to create the MErSiM v1.0 model, we successfully resolved the primary issues plaguing the original version. The MErSiM model eliminates the systematic tropical overestimation, and its predicted global total silicate weathering flux (~3.1 x 10^{12} mol C yr^{-1}) is now in agreement with observations. More fundamentally, this work corrects a structural flaw in the original model, which was unable to simultaneously match the global total flux and the

https://doi.org/10.5194/egusphere-2025-5624
Preprint. Discussion started: 26 January 2026

watershed-scale spatial pattern of weathering. Our improved model achieves its optimal performance at a global flux value consistent with observations, indicating it is not just better calibrated but is more physically coherent and robust. Ultimately, this work delivers a comprehensively evaluated, structurally improved, and observationally constrained model for global silicate weathering. It provides a more trustworthy tool for quantifying the climate sensitivity of the weathering, representing a critical step forward in our ability to simulate the deep-time co-evolution of the solid Earth, its climate, and the global carbon cycle. Specifically, the improved model reveals a profoundly attenuated weathering sensitivity under warm, high-CO_2 conditions. This dampened response, in stark contrast to the original GM09 model, stems from MErSiM's ability to capture the transition toward a more "chemostatic" weathering regime, where fluxes become decoupled from rising temperatures.

https://doi.org/10.5194/egusphere-2025-5624
Preprint. Discussion started: 26 January 2026

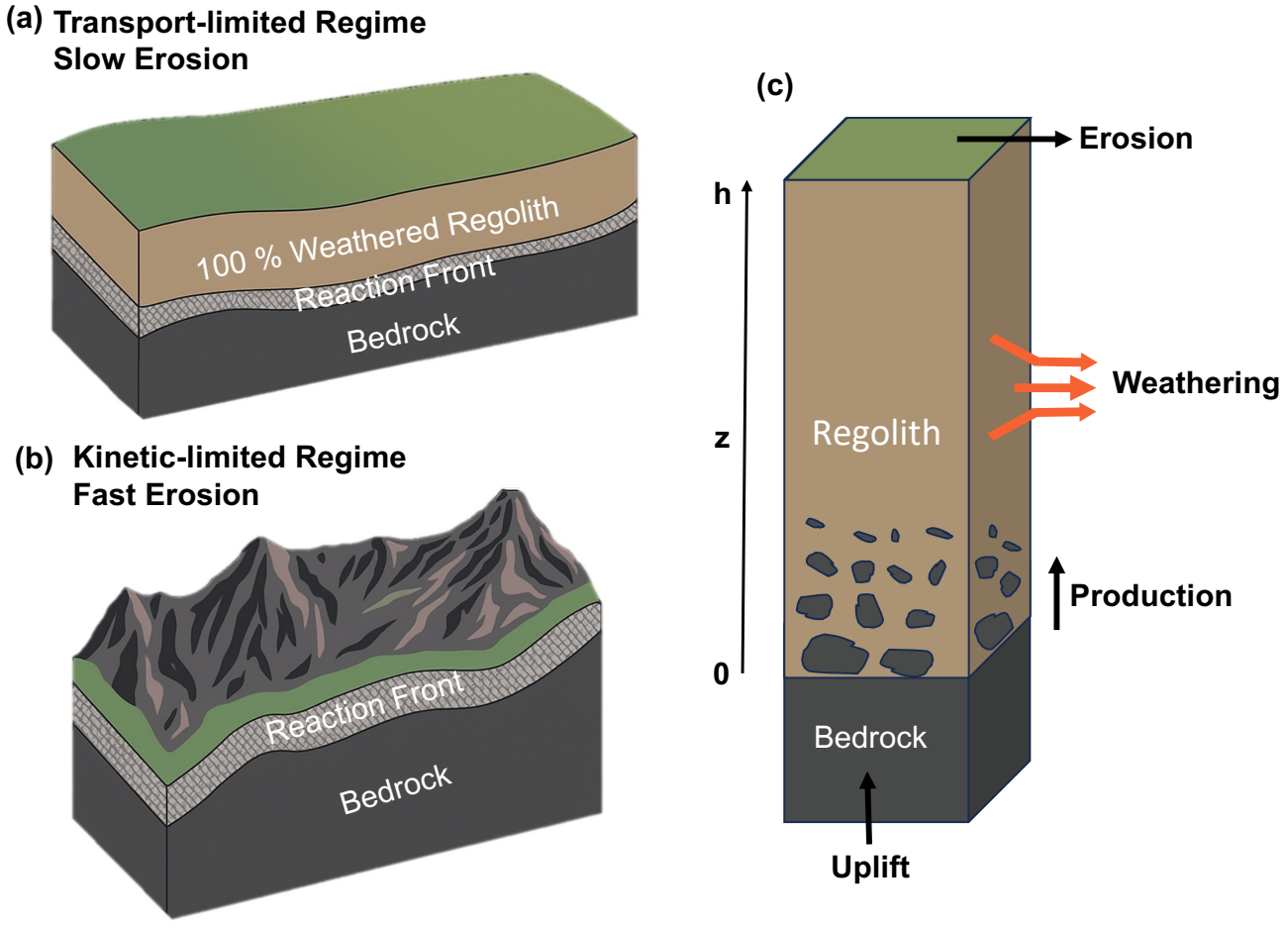

Figure 1: Conceptual diagram of the core of the GM09 model.

(a) Transport-limited regime, usually in flat regions, where the weathering rate is constraint by how fast fresh rock is exposed. (b) Kinetic-limited regime, mostly in steep mountainous regions, where the weathering rate is mostly constraint by how fast the chemical reaction could happen. (c) A schematic representation of GM09 in a single profile at steady state. Rock particles leave the unweathered bedrock at the production rate and pass vertically through the clastic rock at a height of h. In the steady state, the amount of rock production and physical erosion are equal.

https://doi.org/10.5194/egusphere-2025-5624
Preprint. Discussion started: 26 January 2026

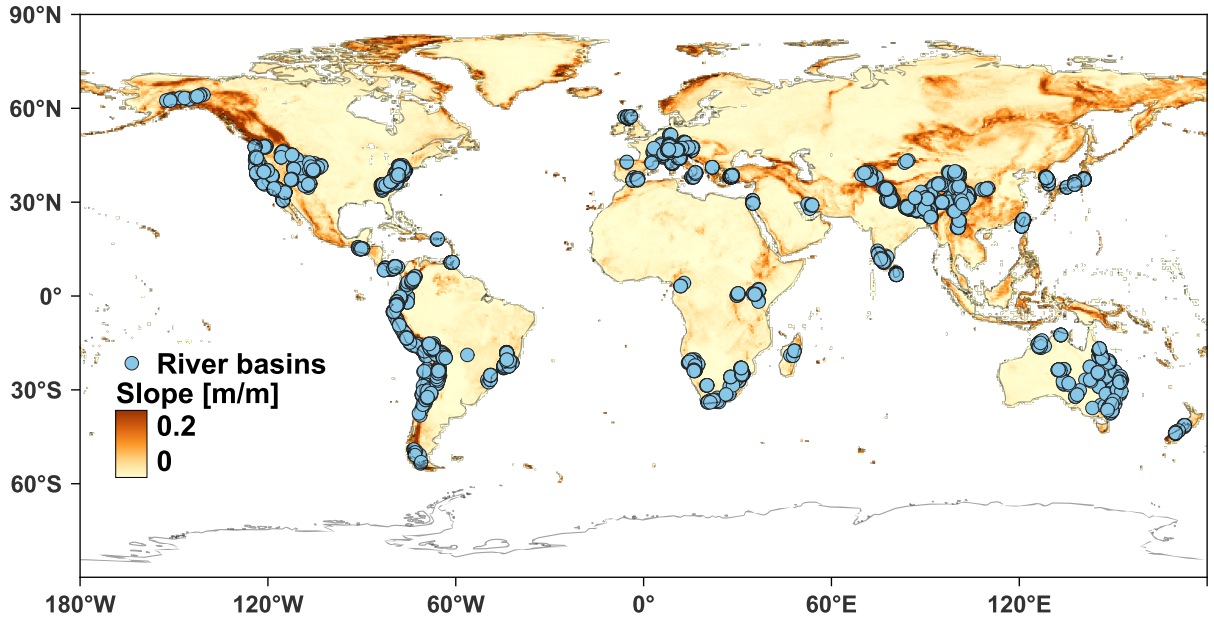

630 **Figure 2: The geographical extent and distribution of global Be isotope erosion rate dataset.**

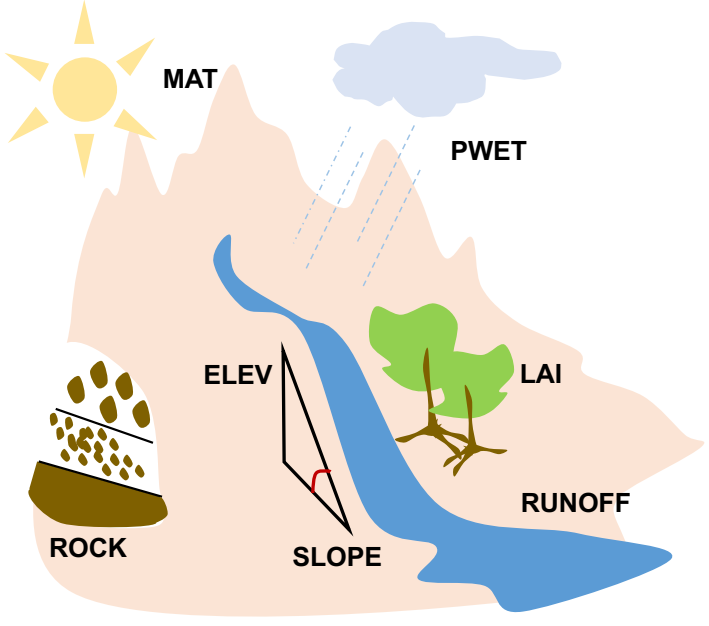

Figure 3: Cartoon showing the environmental factors that influence denudation rates.

https://doi.org/10.5194/egusphere-2025-5624
Preprint. Discussion started: 26 January 2026

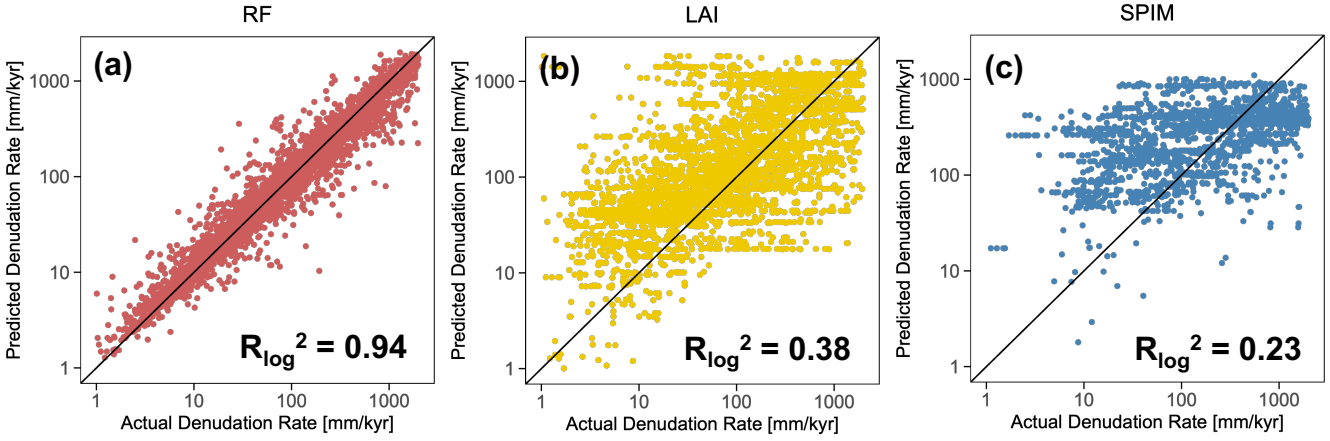

Figure 4: Scatter of predicted basin denudation rates by different methods vs. observations from OCTOPUS.

The observed erosion rates are plotted against the model-predicted rates (y-axis) for (a) our Random Forest (RF) model, (b) the LAI-modified model from Zuo et al. (2024), (c) the original SPIM from Park et al. (2020). The diagonal line represents the 1:1 relationship. Both axes are on a logarithmic scale to accommodate the multi-order-of-magnitude range of erosion rates observed globally. The coefficient of determination for the logarithmic values (R_{log}^2) is used as the primary metric of performance, indicating the proportion of variance in the observed data that is explained by the model. All the inputs of these models are from the same compilation of basin-average variable values.

https://doi.org/10.5194/egusphere-2025-5624
Preprint. Discussion started: 26 January 2026

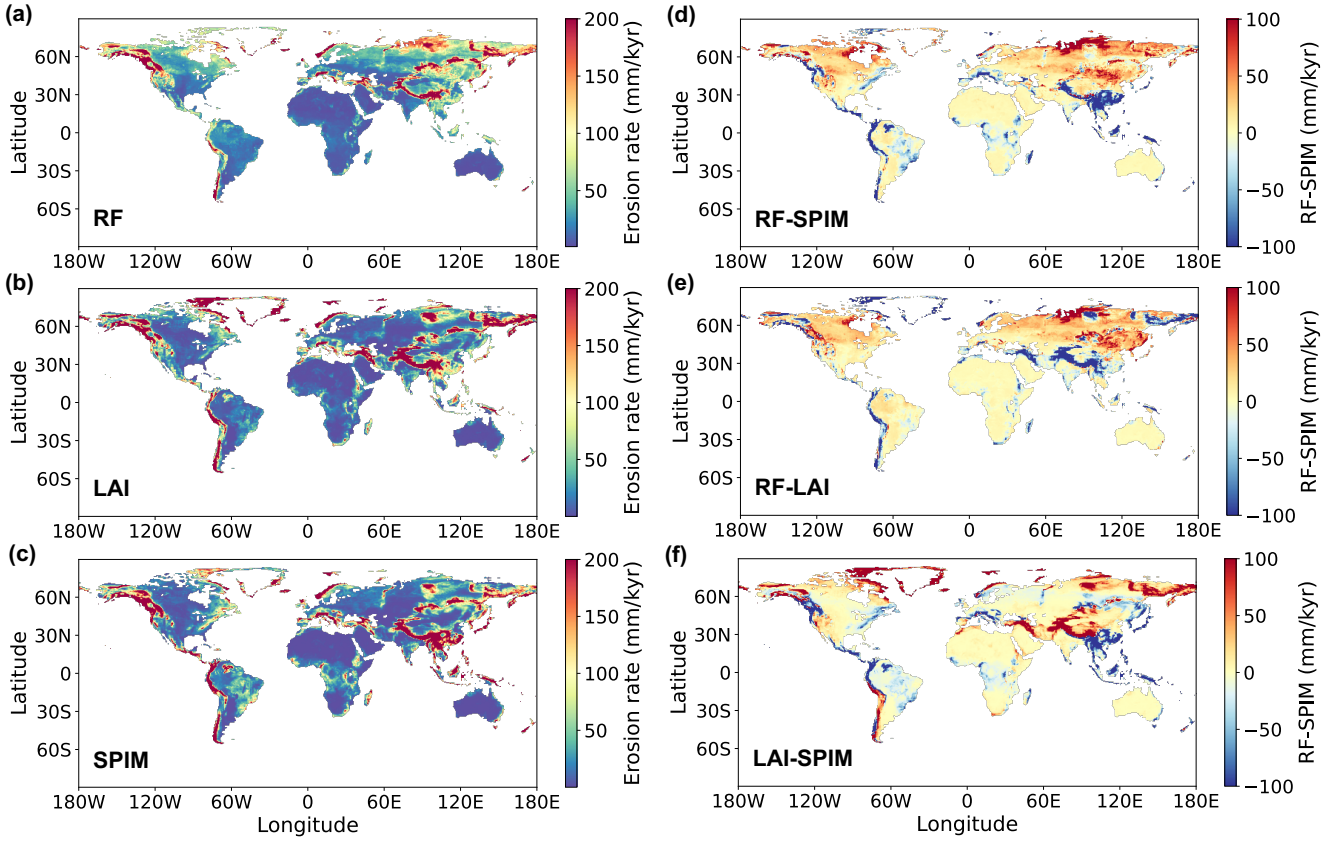

Figure 5: Global erosion rate map calculated by different erosion models and their differences.

(a) Global erosion rate map with 0.5 degree by 0.5-degree resolution calculated from our random forest model (RF). (b) Global erosion rate map calculated from the LAI-modified erosion model by Zuo et al. (2024) (denoted as LAI). (c) Global erosion rate map calculated from the Stream Power Incision Law model (SPIM), with parameters from Park et al. (2020). Global erosion rate map Rates exceeding 200 mm/kyr are still depicted in dark red. (d) Difference between RF and SPIM-calculated erosion rates, with RF predicting significantly lower values in the tropics and the steepest mountainous regions. (d) Difference between RF and LAI-calculated erosion rates. (e) Difference between LAI and SPIM-calculated erosion rates.

https://doi.org/10.5194/egusphere-2025-5624
Preprint. Discussion started: 26 January 2026

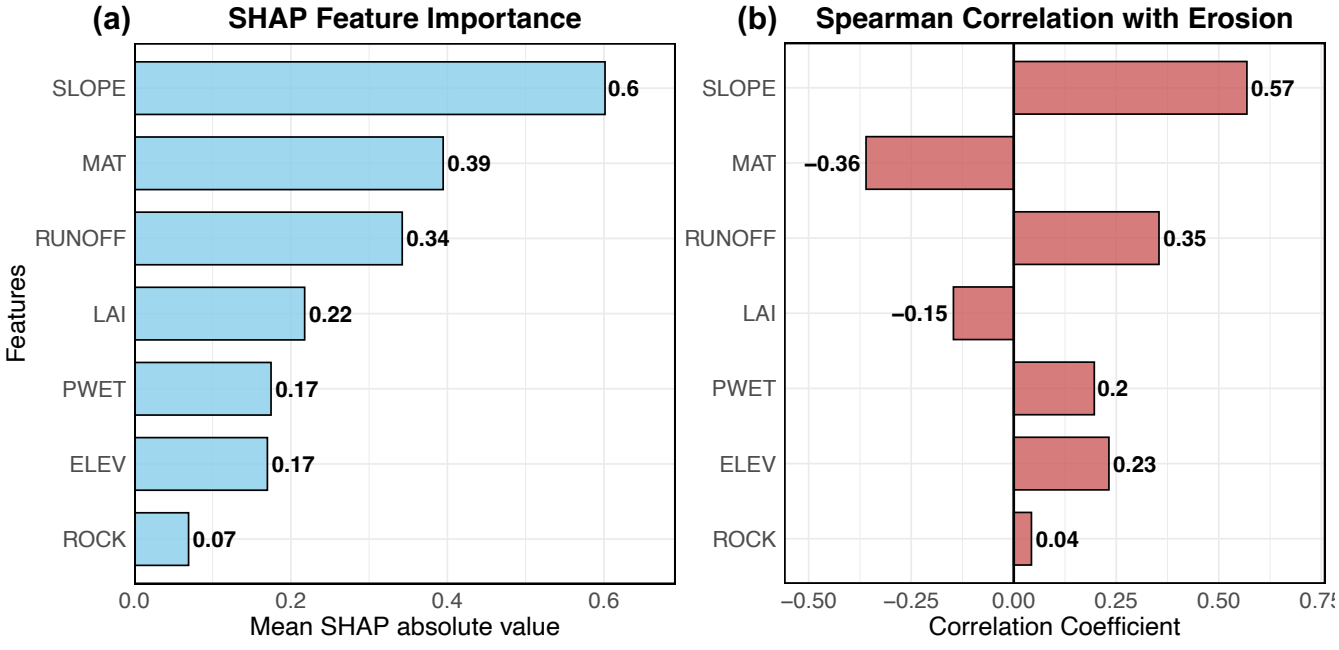

Figure 6: Importance and correlation of predictor variables.

(a) Importance ranking of feature variables for predicting erosion rates shown by mean SHAP absolute value. (b) Spearman rank correlations of each variable against erosion rate.

https://doi.org/10.5194/egusphere-2025-5624
Preprint. Discussion started: 26 January 2026

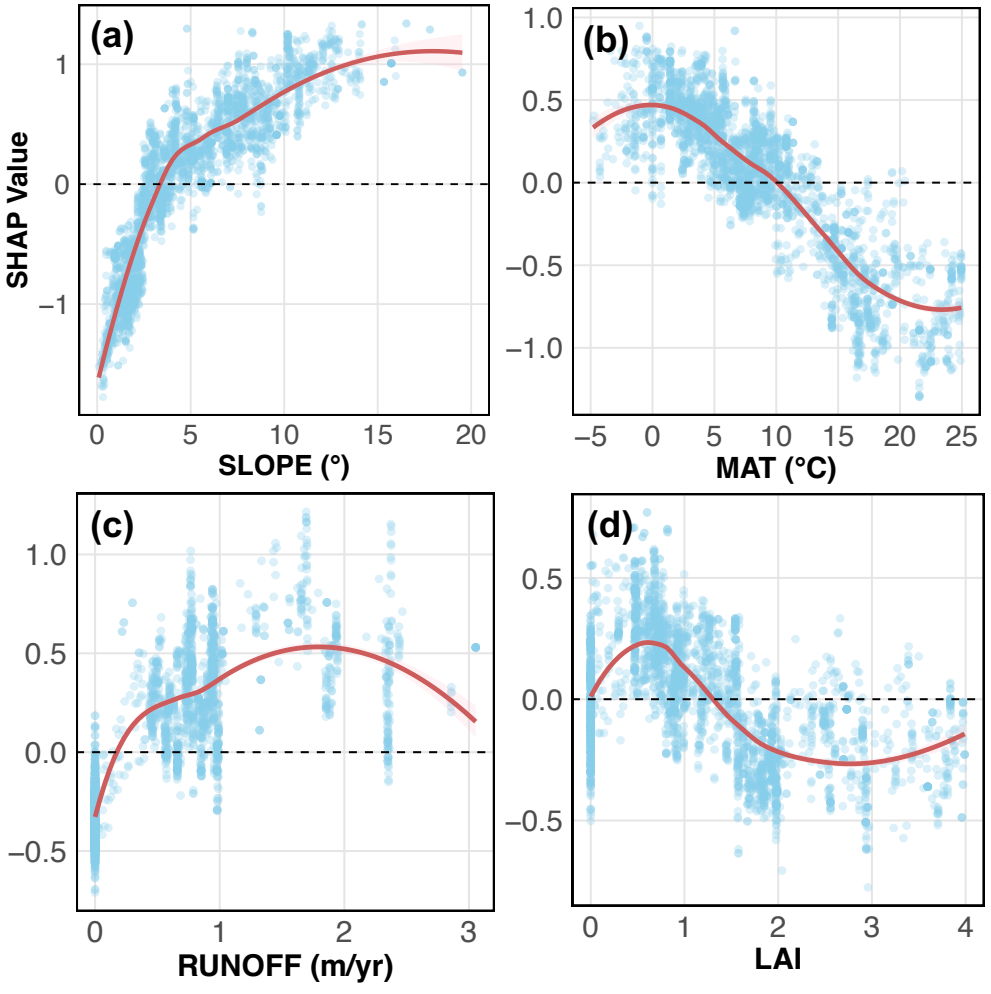

Figure 7: SHAP dependence plots for the 4 main predictor variables used in the Random Forest erosion model.

Each point represents a single river basin from the training dataset. The SHAP value quantifies the feature's contribution to the final prediction for that specific watershed in units of logarithmic erosion rate. Positive SHAP values indicate a contribution that increases the predicted erosion rate, while negative values indicate a contribution that decreases it. The red line is a LOESS smooth curve illustrating the average trend, with the shaded area representing the confidence interval. The plots reveal the complex, non-linear marginal effect of each variable on the model's predictions, such as (a) the saturating effect of high SLOPE, (c) the influence of MAT reflecting frost-cracking in cold regions, (c) the hump-shaped impact of RUNOFF, and (d) bimodal effect of vegetation LAI.

https://doi.org/10.5194/egusphere-2025-5624
Preprint. Discussion started: 26 January 2026

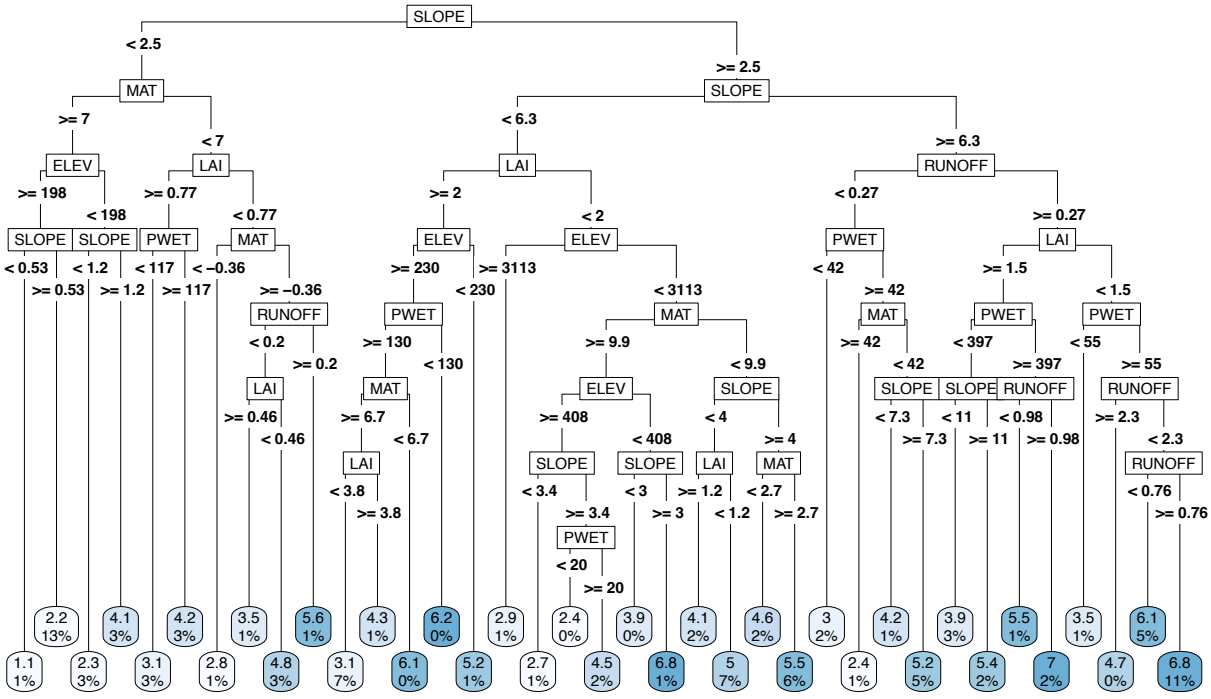

Figure 8: An example decision tree trained on training dataset (random 80% of the whole dataset).

Branch lines show bifurcation thresholds; end nodes display logarithms of predicted denudation rates and proportions of all samples.

https://doi.org/10.5194/egusphere-2025-5624
Preprint. Discussion started: 26 January 2026

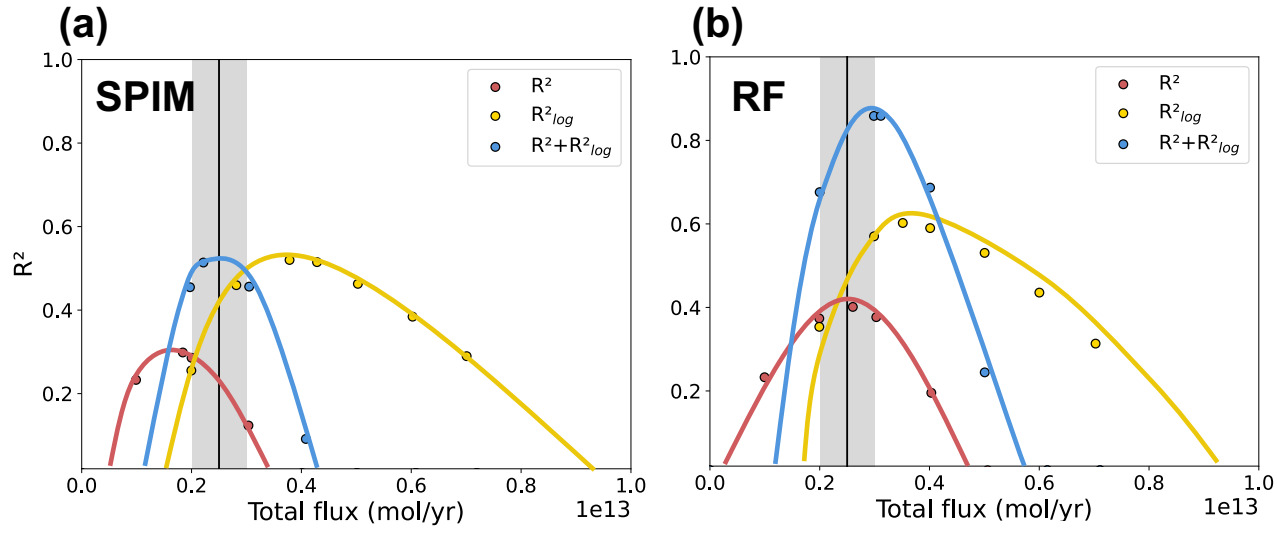

Figure 9: Result of parameter tests for GM09-SPIM and MErSiM.

(a) The R^2 (red), R^2_{log}(yellow), and $R^2 + R^2_{log}$ (blue) of all possible combinations of the parameters. Instead of showing all the dots, only the envelopes (one for each color) are shown for the sake of clearness; the envelopes are obtained by curve fitting (cubic spline interpolation), and the data points used to do the fitting are still shown in the figure. (b) is the same as panel (a), except that the erosion module is replaced by random forest results. The black vertical line and grey zone show the observed weathering flux and its uncertainty range.

https://doi.org/10.5194/egusphere-2025-5624
Preprint. Discussion started: 26 January 2026

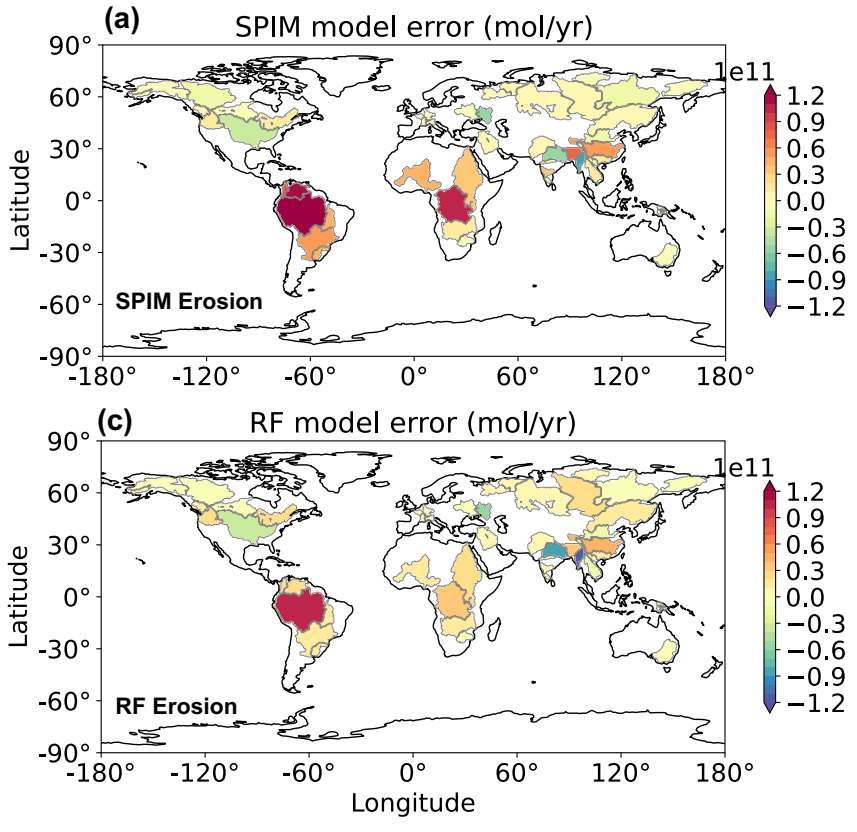

Figure 10: The difference (model − observation) in silicate weathering fluxes for 81 large rivers.

(a) The distribution of model-obsevation difference of original GM09-SPIM model. (c) is the same as panel (a), except that the erosion module is replaced by random forest results. (b)/(d) The scatter plot of model-observation difference.

https://doi.org/10.5194/egusphere-2025-5624
Preprint. Discussion started: 26 January 2026

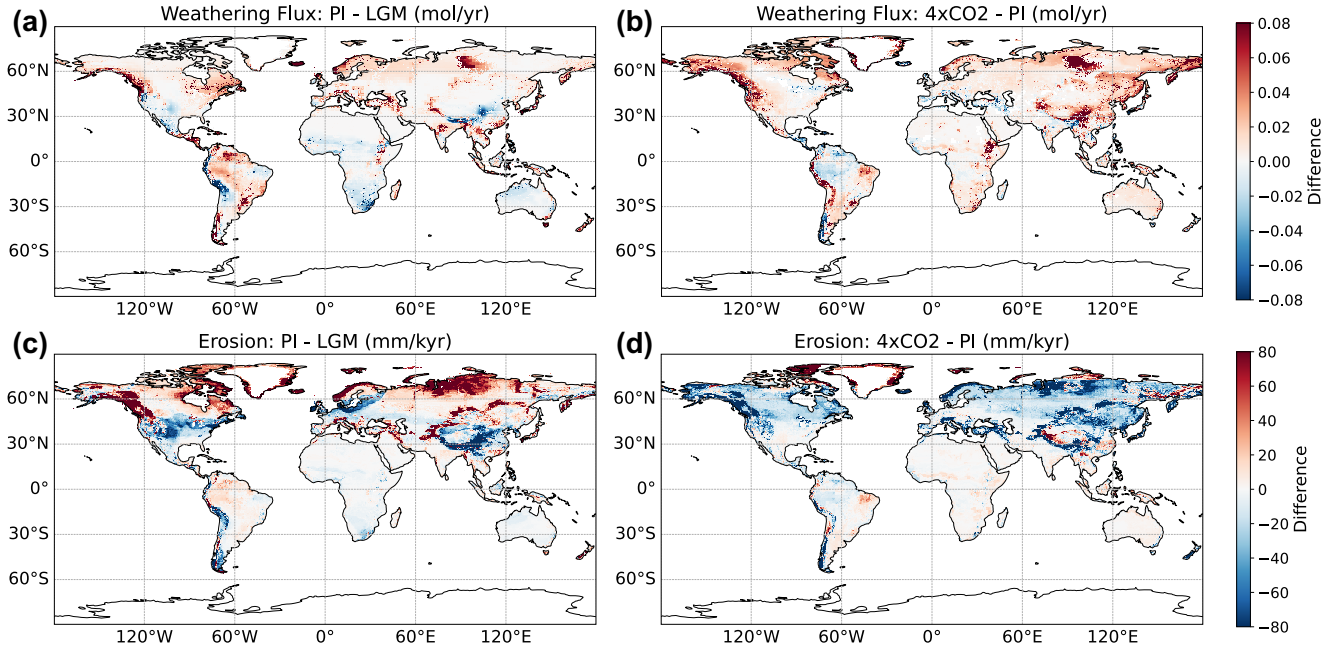

Figure 11: The difference of weathering and erosion for climate scenarios.

(a) Difference of MErSiM modelled PI weathering flux from LGM weathering flux (mol/yr). (b) Difference of MErSiM modelled abrupt 4xCO2 scenario weathering flux from PI weathering flux (mol/yr). (c) Difference of RF modelled PI erosion rate from LGM erosion rate (mm/kyr). (d) Difference of RF modelled abrupt 4xCO2 scenario erosion rate from PI erosion rate (mm/kyr)

https://doi.org/10.5194/egusphere-2025-5624
Preprint. Discussion started: 26 January 2026

690 **Table. 1 Summary of experiment sets. R^2 for erosion is calculated on the validation dataset (20% of the total dataset). R^2 for weathering is the highest $R^2 + R^2_{log}$ searched in the parameter space.**

The baseline erosion model includes six basic predictors, namely SLOPE, ELEVATION, MAT, LAI, RUNOFF and ROCK. The optimistic model is marked as bold black values (Pwet_only).

Experiment	PWET	PSEASON	TSEASON	TMIN	MAP	Erosion validation maximum R^2	Weathering validation maximum R^2
Baseline	×	×	×	×	×	0.81	0.75
Pwet_only	√	×	×	×	×	**0.85**	**0.86**
Pseason_only	×	√	×	×	×	0.83	0.70
Tseason_only	×	×	√	×	×	0.83	0.67
Tmin_only	×	×	×	√	×	0.82	0.75
MAP_only	×	×	×	×	√	0.81	0.65
Pwet_Pseason	√	√	×	×	×	0.84	0.71
Pwet_Tseason	√	×	√	×	×	0.83	0.73
Pwet_Tmin	√	×	×	√	×	0.80	0.75
All_added	√	√	√	√	√	0.87	0.68

695

https://doi.org/10.5194/egusphere-2025-5624
Preprint. Discussion started: 26 January 2026

Table. 2 Model parameters and their values to be searched.

The values with (P) represent the optimal parameters selected by Park20. The values with (M) represent the optimal parameters selected by our MErSiM model. The values with (S) represent the optimal parameters refitted for GM09-SPIM using the new evaluation metric in the new parameter space. Although the range of the cation concentration of metamorphic rocks overlaps with the sedimentary rocks, it is constrained so that the former must be larger or equal than the latter during the search.

k_d (unitless)	k_w (unitless)	σ (unitless)	k_{rp} (unitless)	Concentration (mol m^{-3})	
				Metamorphic	Sediment
$\mathbf{5 \times 10^{-6}}$	1×10^{-3}	-0.5	1.2×10^{-3}	1500(M,S)	500
$\mathbf{1 \times 10^{-5}}$	2×10^{-3}	-0.4(P,S)	2×10^{-3}	2000	1000
$\mathbf{2 \times 10^{-5}}$	5×10^{-3}	-0.2	3×10^{-3}	2500(P)	1500(M,S)
$\mathbf{5 \times 10^{-5}}$	1×10^{-2}	-0.1(M)	4×10^{-3}	3000	2000(P)
$\mathbf{1 \times 10^{-4}}$(M)	2×10^{-2}	0	5×10^{-3}	3500	2500
$\mathbf{2 \times 10^{-4}}$(P)	5×10^{-2}	0.1	6×10^{-3}	4000	3000
$\mathbf{5 \times 10^{-4}}$	1×10^{-1}	0.3	7×10^{-3}		
$\mathbf{5 \times 10^{-4}}$(S)	2×10^{-1}(M)		8×10^{-3}		
$\mathbf{1 \times 10^{-3}}$	5×10^{-1}		9×10^{-3}		
$\mathbf{2 \times 10^{-3}}$	1(P,S)		1×10^{-2}(P)		
$\mathbf{5 \times 10^{-3}}$			1.5×10^{-2}		
$\mathbf{1 \times 10^{-2}}$			5×10^{-2}(M,S)		

Table. 3 Sensitivity of global silicate weathering to climate.

Variable		Climate case				
		LGM	PI	Abrupt4 × CO_2	PI-LGM	4 × CO_2-PI
Land surface temperature (K)		278.4	286.6	301.1	8.2	14.5
Global Ca^{2+} + Mg^{2+}	Park20 model	3.10	4.54	11.31	1.44 (46%)	6.77 (149%)
($\times 10^{12}$ mol yr^{-1})	Revised model	2.12	3.11	4.44	0.99 (47%)	1.33 (42%)

https://doi.org/10.5194/egusphere-2025-5624
Preprint. Discussion started: 26 January 2026

Code and Data availability

The source code for MErSiM v1.0, including the R scripts for the erosion module and Python scripts for the weathering module, is available at https://doi.org/10.5281/zenodo.18015309 (Zhao, 2025). The repository includes a detailed User Manual describing the installation and execution steps.

System Requirements

The model consists of scripts written in R (v4.0+) and Python (v3.8+). It requires standard desktop hardware (minimum 8GB RAM recommended). Key dependencies include the randomForest and caret packages for R, and numpy, netCDF4, and pandas for Python.

License

The model code is distributed under the the Creative Commons Attribution license, allowing for reuse and modification with proper citation. All input datasets used in this study (including GLiM lithology, CRU climate data, and OCTOPUS cosmogenic nuclide data) are cited in the main text and are available from their respective original sources or included in the processed format within the Zenodo repository.

Acknowledgments

This work was supported by the National Natural Science Foundation of China (Grant 42488201; 42225606) and National Key Research and Development Program of China (Grant No. 2022YFF0800200).

Author contribution

All authors have contributed to, read, and approved this submitted manuscript in its current form. Specifically, Jiaxi Zhao designed the study, developed the machine learning model and calibrated the silicate weathering model, and wrote the manuscript; Yonggang Liu contributed to manuscript writing and model improvement; all other authors participated in analysis and editing of the manuscript.

https://doi.org/10.5194/egusphere-2025-5624
Preprint. Discussion started: 26 January 2026

Competing interest

The authors declare that they have no conflict of interest.

References

Amiotte Suchet, P., Probst, J., and Ludwig, W.: Worldwide distribution of continental rock lithology: Implications for the atmospheric/soil CO_2 uptake by continental weathering and alkalinity river transport to the oceans, Global Biogeochemical Cycles, 17, 2002GB001891, https://doi.org/10.1029/2002GB001891, 2003.

Anderson, R. S. and Anderson, S. P.: Geomorphology : The Mechanics and Chemistry of Landscapes, 2010.

Berner, R. A.: A model for atmospheric CO 2 over Phanerozoic time, American Journal of Science, 291, 339–376, https://doi.org/10.2475/ajs.291.4.339, 1991.

Berner, R. A. and Caldeira, K.: The need for mass balance and feedback in the geochemical carbon cycle, Geology, 25, 955–956, https://doi.org/10.1130/0091-7613(1997)025%253C0955:TNFMBA%253E2.3.CO;2, 1997.

Berner, R. A., Lasaga, A. C., and Garrels, R. M.: Carbonate-silicate geochemical cycle and its effect on atmospheric carbon dioxide over the past 100 million years, Am. J. Sci.; (United States), 283:7, https://doi.org/10.2475/ajs.283.7.641, 1983.

Binnie, S. A., Phillips, W. M., Summerfield, M. A., and Fifield, L. K.: Tectonic uplift, threshold hillslopes, and denudation rates in a developing mountain range, Geol, 35, 743, https://doi.org/10.1130/G23641A.1, 2007.

Bluth, G. and Kump, L.: Lithologic and Climatologic Controls of River Chemistry, Geochimica Et Cosmochimica Acta, 58, 2341–2359, https://doi.org/10.1016/0016-7037(94)90015-9, 1994.

Brantley, S. L., Shaughnessy, A., Lebedeva, M. I., and Balashov, V. N.: How temperature-dependent silicate weathering acts as Earth's geological thermostat, Science, 379, 382–389, https://doi.org/10.1126/science.add2922, 2023.

Breiman, L.: Random Forests, Machine Learning, 45, 5–32, https://doi.org/10.1023/A:1010933404324, 2001.

Carretier, S., Regard, V., Vassallo, R., Aguilar, G., Martinod, J., Riquelme, R., Pepin, E., Charrier, R., Hérail, G., Farías, M., Guyot, J.-L., Vargas, G., and Lagane, C.: Slope and climate variability control of erosion in the Andes of central Chile, Geology, 41, 195–198, https://doi.org/10.1130/G33735.1, 2013.

Codilean, A. T., Munack, H., Cohen, T. J., Saktura, W. M., Gray, A., and Mudd, S. M.: OCTOPUS: an open cosmogenic isotope and luminescence database, Earth System Science Data, 10, 2123–2139, https://doi.org/10.5194/essd-10-2123-2018, 2018.

Danabasoglu, G., Lamarque, J.-F., Bacmeister, J., Bailey, D. A., DuVivier, A. K., Edwards, J., Emmons, L. K., Fasullo, J., Garcia, R., Gettelman, A., Hannay, C., Holland, M. M., Large, W. G., Lauritzen, P. H., Lawrence, D. M., Lenaerts, J. T. M., Lindsay, K., Lipscomb, W. H., Mills, M. J., Neale, R., Oleson, K. W., Otto-Bliesner, B., Phillips, A. S., Sacks, W., Tilmes, S., van Kampenhout, L., Vertenstein, M., Bertini, A., Dennis, J., Deser, C., Fischer, C., Fox-Kemper, B., Kay, J. E., Kinnison, D., Kushner, P. J., Larson, V. E., Long, M. C., Mickelson, S., Moore, J. K., Nienhouse, E., Polvani, L., Rasch, P. J., and Strand, W. G.: The Community Earth System Model Version 2 (CESM2), Journal of Advances in Modeling Earth Systems, 12, https://doi.org/10.1029/2019MS001916, 2020.

https://doi.org/10.5194/egusphere-2025-5624
Preprint. Discussion started: 26 January 2026

Delunel, R., Van Der Beek, P. A., Carcaillet, J., Bourlès, D. L., and Valla, P. G.: Frost-cracking control on catchment denudation rates: Insights from in situ produced 10Be concentrations in stream sediments (Ecrins–Pelvoux massif, French Western Alps), Earth and Planetary Science Letters, 293, 72–83, https://doi.org/10.1016/j.epsl.2010.02.020, 2010.

DiBiase, R. A. and Whipple, K. X.: The influence of erosion thresholds and runoff variability on the relationships among topography, climate, and erosion rate, https://doi.org/10.1029/2011JF002095, 2011.

Donnadieu, Y., Goddéris, Y., Pierrehumbert, R., Dromart, G., Fluteau, F., and Jacob, R.: A GEOCLIM simulation of climatic and biogeochemical consequences of Pangea breakup, Geochem Geophys Geosyst, 7, 2006GC001278, https://doi.org/10.1029/2006GC001278, 2006.

Farr, T. G., Rosen, P. A., Caro, E., Crippen, R., Duren, R., Hensley, S., Kobrick, M., Paller, M., Rodriguez, E., Roth, L., Seal, D., Shaffer, S., Shimada, J., Umland, J., Werner, M., Oskin, M., Burbank, D., and Alsdorf, D.: The Shuttle Radar Topography Mission, Reviews of Geophysics, 45, 2005RG000183, https://doi.org/10.1029/2005RG000183, 2007.

Fick, S. E. and Hijmans, R. J.: WorldClim 2: new 1-km spatial resolution climate surfaces for global land areas, International Journal of Climatology, 37, 4302–4315, https://doi.org/10.1002/joc.5086, 2017.

Gabet, E. J. and Mudd, S. M.: A theoretical model coupling chemical weathering rates with denudation rates, Geology, 37, 151–154, https://doi.org/10.1130/G25270A.1, 2009.

Gaillardet, J., Dupré, B., Louvat, P., and Allègre, C. J.: Global silicate weathering and CO2 consumption rates deduced from the chemistry of large rivers, Chemical Geology, 159, 3–30, https://doi.org/10.1016/S0009-2541(99)00031-5, 1999.

Godderis, Y., Le Hir, G., Macouin, M., Donnadieu, Y., Hubert-Theou, L., Dera, G., Aretz, M., Fluteau, F., Li, Z. X., and Halverson, G. P.: Paleogeographic forcing of the strontium isotopic cycle in the Neoproterozoic, GONDWANA RESEARCH, 42, 151–162, https://doi.org/10.1016/j.gr.2016.09.013, 2017.

Hales, T. C. and Roering, J. J.: Climatic controls on frost cracking and implications for the evolution of bedrock landscapes, J. Geophys. Res., 112, 2006JF000616, https://doi.org/10.1029/2006JF000616, 2007.

Harris, I., Jones, P., Osborn, T., and Lister, D.: Updated high-resolution grids of monthly climatic observations—The CRU TS3.10 Dataset, International Journal of Climatology, 34, n/a-n/a, https://doi.org/10.1002/joc.3711, 2014.

Hartmann, J. and Moosdorf, N.: The new global lithological map database GLiM: A representation of rock properties at the Earth surface, Geochemistry, Geophysics, Geosystems, 13, https://doi.org/10.1029/2012GC004370, 2012.

Hartmann, J., Jansen, N., Dürr, H. H., Kempe, S., and Köhler, P.: Global CO2-consumption by chemical weathering: What is the contribution of highly active weathering regions?, Global and Planetary Change, 69, 185–194, https://doi.org/10.1016/j.gloplacha.2009.07.007, 2009.

Heimsath, A. M., Dietrich, W. E., Nishiizumi, K., and Finkel, R. C.: The soil production function and landscape equilibrium, Nature, 388, 358–361, https://doi.org/10.1038/41056, 1997.

Hilton, R. G. and West, A. J.: Mountains, erosion and the carbon cycle, Nat Rev Earth Environ, 1, 284–299, https://doi.org/10.1038/s43017-020-0058-6, 2020.

Kump, L. R., Brantley, S. L., and Arthur, M. A.: Chemical Weathering, Atmospheric CO_2, and Climate, Annu. Rev. Earth Planet. Sci., 28, 611–667, https://doi.org/10.1146/annurev.earth.28.1.611, 2000.

https://doi.org/10.5194/egusphere-2025-5624
Preprint. Discussion started: 26 January 2026

Lague, D.: The stream power river incision model: evidence, theory and beyond, Earth Surface Processes and Landforms, 39, 38–61, https://doi.org/10.1002/esp.3462, 2014.

Larsen, I. J. and Montgomery, D. R.: Landslide erosion coupled to tectonics and river incision, Nature Geosci, 5, 468–473, https://doi.org/10.1038/ngeo1479, 2012.

Larsen, I. J., Montgomery, D. R., and Greenberg, H. M.: The contribution of mountains to global denudation, Geology, 42, 527–530, https://doi.org/10.1130/G35136.1, 2014.

Lawrence, P. and Chase, T.: Representing a new MODIS consistent land surface in the Community Land Model (CLM 3.0), Journal of Geophysical Research, 112, https://doi.org/10.1029/2006JG000168, 2007.

Li, X., Hu, Y., Guo, J., Lan, J., Lin, Q., Bao, X., Yuan, S., Wei, M., Li, Z., Man, K., Yin, Z., Han, J., Zhang, J., Zhu, C., Zhao, Z., Liu, Y., Yang, J., and Nie, J.: A high-resolution climate simulation dataset for the past 540 million years, Sci Data, 9, 371, https://doi.org/10.1038/s41597-022-01490-4, 2022.

Lundberg, S. and Lee, S.-I.: A Unified Approach to Interpreting Model Predictions, https://doi.org/10.48550/ARXIV.1705.07874, 2017.

Maher, K. and Chamberlain, C. P.: Hydrologic Regulation of Chemical Weathering and the Geologic Carbon Cycle, Science, 343, 1502–1504, https://doi.org/10.1126/science.1250770, 2014.

Milliman, J. D. and Syvitski, J. P. M.: Geomorphic/tectonic control of sediment discharge to the ocean: the importance of small mountainous rivers, Journal of Geology, 100, 525–544, https://doi.org/10.1086/629606, 1992.

Mills, B. J. W., Donnadieu, Y., and Goddéris, Y.: Spatial continuous integration of Phanerozoic global biogeochemistry and climate, Gondwana Research, 100, 73–86, https://doi.org/10.1016/j.gr.2021.02.011, 2021.

Mishra, A. K., Placzek, C., and Jones, R.: Coupled influence of precipitation and vegetation on millennial-scale erosion rates derived from 10Be, PLoS One, 14, e0211325, https://doi.org/10.1371/journal.pone.0211325, 2019.

Moon, S., Chamberlain, C. P., and Hilley, G. E.: New estimates of silicate weathering rates and their uncertainties in global rivers, Geochimica et Cosmochimica Acta, 134, 257–274, https://doi.org/10.1016/j.gca.2014.02.033, 2014.

Moquet, J.-S., Crave, A., Viers, J., Seyler, P., Armijos, E., Bourrel, L., Chavarri, E., Lagane, C., Laraque, A., Lavado Casimiro, W. S., Pombosa, R., Noriega, L., Vera, A., and Guyot, J.-L.: Chemical weathering and atmospheric/soil CO2 uptake in the Andean and Foreland Amazon basins, CHEMICAL GEOLOGY, 287, 1–26, https://doi.org/10.1016/j.chemgeo.2011.01.005, 2011.

Moquet, J.-S., Guyot, J.-L., Crave, A., Viers, J., Filizola, N., Martinez, J.-M., Oliveira, T. C., Sánchez, L. S. H., Lagane, C., Casimiro, W. S. L., Noriega, L., and Pombosa, R.: Amazon River dissolved load: temporal dynamics and annual budget from the Andes to the ocean, Environ Sci Pollut Res, 23, 11405–11429, https://doi.org/10.1007/s11356-015-5503-6, 2016.

Mudd, S. M., Harel, M.-A., Hurst, M. D., Grieve, S. W. D., and Marrero, S. M.: The CAIRN method: automated, reproducible calculation of catchment-averaged denudation rates from cosmogenic nuclide concentrations, Earth Surface Dynamics, 4, 655–674, https://doi.org/10.5194/esurf-4-655-2016, 2016.

Müller, R. D., Mather, B., Dutkiewicz, A., Keller, T., Merdith, A., Gonzalez, C. M., Gorczyk, W., and Zahirovic, S.: Evolution of Earth's tectonic carbon conveyor belt, Nature, 605, 629–639, https://doi.org/10.1038/s41586-022-04420-x, 2022.

https://doi.org/10.5194/egusphere-2025-5624
Preprint. Discussion started: 26 January 2026

Ouimet, W. B., Whipple, K. X., and Granger, D. E.: Beyond threshold hillslopes: Channel adjustment to base-level fall in tectonically active mountain ranges, Geology, 37, 579–582, https://doi.org/10.1130/G30013A.1, 2009.

Park, Y., Maffre, P., Goddéris, Y., Macdonald, F. A., Anttila, E. S. C., and Swanson-Hysell, N. L.: Emergence of the Southeast Asian islands as a driver for Neogene cooling, Proc. Natl. Acad. Sci. U.S.A., 117, 25319–25326, https://doi.org/10.1073/pnas.2011033117, 2020.

Perron, J. T.: Climate and the Pace of Erosional Landscape Evolution, Annu. Rev. Earth Planet. Sci., 45, 561–591, https://doi.org/10.1146/annurev-earth-060614-105405, 2017.

Portenga, E. W. and Bierman, P. R.: Understanding Earth's eroding surface with 10Be, GSAT, 21, 4–10, https://doi.org/10.1130/G111A.1, 2011.

Prosser, I. P., Dietrich, W. E., and Stevenson, J.: Flow resistance and sediment transport by concentrated overland flow in a grassland valley, Geomorphology, 13, 71–86, https://doi.org/10.1016/0169-555X(95)00020-6, 1995.

Raymo, M. E. and Ruddiman, W.: Cooling in the late Cenozoic [14], Nature, 361, 124, https://doi.org/10.1038/361124a0, 1993.

Riebe, C. S., Kirchner, J. W., Granger, D. E., and Finkel, R. C.: Strong tectonic and weak climatic control of long-term chemical weathering rates, Geol, 29, 511, https://doi.org/10.1130/0091-7613(2001)029%253C0511:STAWCC%253E2.0.CO;2, 2001.

Rugenstein, J. K. C., Ibarra, D. E., Zhang, S., Planavsky, N. J., and Von Blanckenburg, F.: Isotope mass-balance constraints preclude that mafic weathering drove Neogene cooling, Proc. Natl. Acad. Sci. U.S.A., 118, e2026345118, https://doi.org/10.1073/pnas.2026345118, 2021.

Scotese, C. R.: An atlas of phanerozoic paleogeographic maps: The seas come in and the seas go out, 679–728 pp., 2021.

Shapley, L. S.: 17. A Value for n-Person Games, in: Contributions to the Theory of Games (AM-28), Volume II, edited by: Kuhn, H. W. and Tucker, A. W., Princeton University Press, 307–318, https://doi.org/10.1515/9781400881970-018, 1953.

Snyder, N. P., Whipple, K. X., Tucker, G. E., and Merritts, D. J.: Importance of a stochastic distribution of floods and erosion thresholds in the bedrock river incision problem, J. Geophys. Res., 108, 2001JB001655, https://doi.org/10.1029/2001JB001655, 2003.

Tucker, G. E.: Drainage basin sensitivity to tectonic and climatic forcing: implications of a stochastic model for the role of entrainment and erosion thresholds, Earth Surf Processes Landf, 29, 185–205, https://doi.org/10.1002/esp.1020, 2004.

Valdes, P. J., Scotese, C. R., and Lunt, D. J.: Deep ocean temperatures through time, Clim. Past, 17, 1483–1506, https://doi.org/10.5194/cp-17-1483-2021, 2021.

Walker, J. C. G., Hays, P. B., and Kasting, J. F.: A negative feedback mechanism for the long-term stabilization of Earth's surface temperature., Journal of Geophysical Research, 86, 9776–9782, https://doi.org/10.1029/JC086iC10p09776, 1981.

Wan, S., Clift, P. D., Li, A., Yu, Z., Li, T., and Hu, D.: Tectonic and climatic controls on long-term silicate weathering in Asia since 5 Ma, Geophysical Research Letters, 39, 2012GL052377, https://doi.org/10.1029/2012GL052377, 2012.

West, A., Galy, A., and Bickle, M.: Tectonic and climatic controls on silicate weathering, Earth and Planetary Science Letters, 235, 211–228, https://doi.org/10.1016/j.epsl.2005.03.020, 2005.

https://doi.org/10.5194/egusphere-2025-5624
Preprint. Discussion started: 26 January 2026

White, A. F. and Blum, A. E.: Effects of climate on chemical_ weathering in watersheds, Geochimica et Cosmochimica Acta, 59, 1729–1747, https://doi.org/10.1016/0016-7037(95)00078-E, 1995.

White, A. F. and Brantley, S. L.: The effect of time on the weathering of silicate minerals: Why do weathering rates differ in the laboratory and field?, Chemical Geology, 202, 479–506, https://doi.org/10.1016/j.chemgeo.2003.03.001, 2003.

Willenbring, J. K., Codilean, A. T., Ferrier, K. L., McElroy, B., and Kirchner, J. W.: Short Communication: Earth is (mostly) flat, but mountains dominate global denudation: apportionment of the continental mass flux over millennial time scales, revisited, https://doi.org/10.5194/esurfd-2-1-2014, 29 January 2014.

Zhang, M., Liu, Y., Zhu, J., Wang, Z., and Liu, Z.: Impact of Dust on Climate and AMOC During the Last Glacial Maximum Simulated by CESM1.2, Geophysical Research Letters, 49, e2021GL096672, https://doi.org/10.1029/2021GL096672, 2022.

Zhao, J., Liu, Y., Li, G., and Zuo, H.: Thresholds in the controls of denudation rates: A global analysis of tectonic, climatic and biological factors based on machine learning, Earth and Planetary Science Letters, 674, 119750, https://doi.org/10.1016/j.epsl.2025.119750, 2026.

Zuo, H., Liu, Y., Li, G., Xu, Z., Zhao, L., Guo, Z., and Hu, Y.: A revised model of global silicate weathering considering the influence of vegetation cover on erosion rate, Geosci. Model Dev., 17, 3949–3974, https://doi.org/10.5194/gmd-17-3949-2024, 2024.